Cite as: S. Loomba *et al.*, *Science* 10.1126/science.abo0924 (2022).

Connectomic comparison of mouse and human cortex

Sahil Loomba[1,2]†, Jakob Straehle[1]†‡§, Vijayan Gangadharan[1]†¶, Natalie Heike[1]†, Abdelrahman Khalifa[1]†, Alessandro Motta[1]†, Niansheng Ju[1], Meike Sievers[1,2], Jens Gempt[3], Hanno S. Meyer[3], Moritz Helmstaedter[1]*

[1]Department of Connectomics, Max Planck Institute for Brain Research, Frankfurt, Germany. [2]Faculty of Science, Radboud University, Nijmegen, Netherlands. [3]Department of Neurosurgery, Klinikum rechts der Isar, School of Medicine, Technical University of Munich, Germany.

†These authors contributed equally to this work.

‡Present address: Department of Neurosurgery, University Freiburg, Freiburg, Germany.

§Present address: Berta-Ottenstein Clinician Scientist Program, Faculty of Medicine, University Freiburg, Freiburg, Germany.

¶Present address: Institute for Beta Cell Biology, German Diabetes Center, Leibniz Center for Diabetes Research at Heinrich Heine University Düsseldorf, Düsseldorf, Germany.

***Corresponding author. E-mail: mh@brain.mpg.de**

The human cerebral cortex houses 1,000 times more neurons than the cerebral cortex of a mouse, but the possible differences in synaptic circuits between these species are still poorly understood. We used 3-dimensional electron microscopy of mouse, macaque and human cortical samples to study their cell type composition and synaptic circuit architecture. The 2.5-fold increase in interneurons in humans compared to mouse was compensated by a change in axonal connection probabilities and therefore did not yield a commensurate increase in inhibitory-vs-excitatory synaptic input balance on human pyramidal cells. Rather, increased inhibition created an expanded interneuron-to-interneuron network, driven by an expansion of interneuron-targeting interneuron types and an increase in their synaptic selectivity for interneuron innervation. These constitute key neuronal network alterations in human cortex.

The human brain, with its 86 billion nerve cells (*1*) forming a network of unparalleled complexity, is of special interest for neuroscience. Yet, over the last 50 years, rodents (in particular the mouse) have emerged as key research subjects, offering methodological opportunities not available for the study of the human brain. Because at the molecular level, evolutionary homology is substantial for ion channels, synaptic receptors, and other key molecular constituents of the brain, similar homology has been assumed for neuronal circuits, especially in the cerebral cortex. However, comparative synaptic-resolution connectomic studies of mouse and human cortex are required to determine the degree to which circuit structure may have evolved between species.

Detailed studies of the human cerebral cortex have provided data on cellular composition of the neuropil (*1–14*), synaptic properties (*15–25*) and neuronal morphology (*14*, *26–28*), yielding a comparative description with reference to rodents that indicates a larger number of glial cells (*2*), larger synapses (*20*, *29*, *30*), and more inhibitory interneurons (*4*, *9*) to form the neuronal network of the human cortex. This latter comparison had been confounded by rodent data reporting an interneuron fraction of 8-25%, (*3*, *4*, *31–37*), thus potentially on par with data from primates (range 15-37%, (*38–42*)). Recent transcriptomic data substantiates an at least 2-fold increase (*4*, *9*), suggesting the balance between inhibitory and excitatory synapses to be substantially shifted toward inhibition. Furthermore, based on the about 3-fold larger extent of the dendritic trees of human pyramidal cells, it has been assumed that human cortical neurons receive substantially more synapses than those of rodents (e.g., 10,000 in rodents vs 30,000 in human, (*29*, *43–46*)).

However, a circuit-level analysis of human cortex that addresses the potential effect of multi-fold increased inhibitory circuit elements is still missing. Would, as a result, the inhibitory-to-excitatory synaptic balance be increased in the human cortex? Because inhibitory-to excitatory synaptic balance has emerged as a key set point that might be altered in neuropsychiatric diseases (studied primarily in mouse models, (*47*, *48*)), this question is relevant for the healthy and diseased human brain.

We used 3-dimensional electron microscopy followed by sparse and dense circuit reconstruction (*49*) to map the synaptic and cellular composition of layer 2/3 in mouse, macaque and human cortex. Sampling from multiple individuals and cortical regions, we screened for key connectomic alterations between mouse and human cortex, which a single dataset from a given human individual and disease condition would not have allowed (*10*). While our human data was from diseased individuals who underwent neurosurgical interventions, the patients had not undergone yearlong treatment for epileptic disorders that could have substantially altered the synaptic network. By including additional data from macaque in our study, we furthermore could ensure that none of the reported effects was exclusively attributable to a

diseased state of the human brain. We determined the circuit effects of an expanded inhibitory neuron population in human cortex and obtained a quantitative picture of the human pyramidal cell synaptic input architecture.

Results

We obtained tissue samples (Fig. 1) from the cerebral cortex of two human individuals (a 69-year-old female and an 80-year-old male) who underwent neurosurgical operations (access tissue that had to be removed during surgery and would have been discarded otherwise) (Materials and methods) and of one rhesus macaque (Macaca mulatta, 15.6-year old male). Individual age corresponded to 83%, 102% and 52% of statistical life expectancy, respectively.

From these tissue samples, we acquired 3-D electron microscopy (EM) image datasets in cortical layer 2/3 (L2/3) using either serial blockface EM (SBEM) ((*50*), macaque primary somatosensory cortex (S1) dataset sized 176x224x100 μm^3; superior temporal gyrus (STG) sized 175x225x108 μm^3; human (H5) STG sized 166x216x112 μm^3 and human (H6) inferior frontal gyrus sized 170x215x79 μm^3, all at a voxel size of 11.24x11.24x(28-30) nm^3) or ATUM-multiSEM ((*51–53*), dataset human (H5) STG spanning all cortical layers, sized 1.7 mm × 2.1 mm × 28.3 µm and dataset from the same sample focused on L2/3 sized 1.1 mm × 1.1 mm × 82 µm (total 0.41 PB of data) both at a voxel size of 4x4x(35-40)nm^3). For comparison with mouse cortex, we densely reconstructed (*49*, *54*) previously published 3D EM datasets from L2/3 of S1, V2, PPC and ACC cortical areas (*55*) and acquired an additional dataset from mouse A2 cortex sized 115x175x109 μm^3, approximately corresponding to the location of the STG datasets from macaque and human. In the following, we report effects that were multi-fold between mouse (n=5 individuals, n=5 cortical regions) and macaque/human (n=3 individuals, n=4 cortical regions).

Inhibitory vs. excitatory neuronal composition

The fraction of nerve cells that were interneurons (INs), increased 2.5-fold between mouse and macaque/human [n=88 of 734 vs. 278 of 914 neurons from n=5 mouse and n=4 macaque/human datasets pooled, P<0.001 (Methods)] (Fig. 2, A and B), consistent with recent reports from transcriptomic cell type analyses, (*4*, *9*). This change in the neuronal composition of cortical tissue could have profound effects on the synaptic input to pyramidal (excitatory) neurons (ExNs, Fig. 2C): If all other circuit properties were unchanged between mouse and human, the inhibitory-to-excitatory balance (i/e balance) would also be 2.5-fold shifted toward inhibition compared to mouse.

Synaptic inputs to pyramidal cell dendrites

We therefore first analyzed the synaptic input to pyramidal cell dendrites in mouse, macaque and human (Fig. 2, D to H). While the density of synapses onto the dendritic shaft of pyramidal cells remained largely constant from mouse to macaque and only slightly increased in human [0.16 ± 0.13 per µm of dendritic shaft length vs. 0.17 ± 0.11 and 0.21 ± 0.08; = 46, 36, 49; P = 0.6 and P = .003 for mouse to macaque and mouse to human, respectively, Kolmogorov–Smirnov (KS) test; mean±s.d.]; (Fig. 2, D and E), synapses onto dendritic spines were 2.7-fold sparser in macaque and human (1.99 ± 0.65 per µm of dendritic shaft length (mouse) vs. 0.86 ± 0.36 (macaque) and 0.67 ± 0.25 (human); mean±s.d.; n=46,36,49, respectively; $P<10^{-18}$, KS test mouse vs. macaque and human) (Fig. 2, D and E). As a result, the fraction of synapses made onto the dendritic shafts of pyramidal cells (out of all input synapses to these dendrites) was increased 2.7-fold (n=1111 synapses, mouse and n=1638 synapses macaque and human, P<0.001, KS test) (Fig. 2, F and H). Synaptic inputs to spine necks, stubs or double innervation of dendritic spines were rare but slightly increased in macaque and human (Fig. 2G, statistics are provided in caption).

In mouse, synapses onto dendritic spines have been reported to be predominantly excitatory (*49*, *56*) and synapses onto dendritic shafts predominantly inhibitory (*55*, *57*, *58*). Therefore, the finding of a 2.7-fold increased fraction of shaft synapses could indicate a substantial shift in the set point for the i/e balance in human [as recently claimed for nonhuman primate (*59*)]. For this to be correct, however, the properties of excitatory and inhibitory axons, in particular their preference for establishing synapses onto dendritic shafts and spines, would have to remain unaltered between mouse and macaque and human. This we investigated next (Figs. 3 and 4).

Synaptic properties of excitatory and inhibitory neurons

We first reconstructed axons of pyramidal cells and interneurons in mouse and human (Fig. 3, A to C) to determine their synaptic preferences. The rate of spine innervation showed the well-documented dichotomy in mouse (Fig. 3, A and B) (*49*, *55*, *60*): pyramidal cell axons targeted dendritic spines with 61.47 ± 9.26% (mean±s.d.) of their output synapses (n=11 axons, n=367 output synapses), while interneurons only very rarely made an output synapses as the only synapse onto a dendritic spine (n=1 of 263 IN output synapses in mouse), with no overlap between the populations. In human, however, axons reconstructed from the cell bodies of pyramidal cells made only 30.37 ± 16.16% (mean±s.d.) of their output synapses onto dendritic spines (n=15 axons, n=1126 output synapses), while interneurons maintained their almost complete exclusion of single spine innervation (Fig.

3B,C; n=12 axons, n=345 output synapses, of which n=1 were single spine synapses; note that interneuron axons did however innervate dendritic spines as double innervations, in all species, as reported for subtypes of interneurons, (fig. S3) (*61–63*); Note further that only the single spine innervation rate was used for the following analyses,). Thus the distributions of synaptic target properties between pyramidal and interneuron axons reconstructed from their cell body of origin were less separated in human (Fig. 3B) and indicated a change in axonal synaptic preference from mouse to human.

In the dense cortical neuropil, only a fraction of axons originates from neurons whose cell body is located in close proximity, while most have more distal origins. To study the target properties of all axons in the neuropil, also those without their cell body of origin in the data set, we next analyzed the dense population of axons in mouse vs. macaque and human that we obtained from the dense automated reconstructions (n=202,954 axons total with n=1,618,129 output synapses) (Fig. 3, D to F). Mouse axons predominantly innervated spines (Fig. 3E), as expected from the soma-based reconstructions (Fig. 3B) and the small fraction of interneurons (Fig. 2B). Densely sampled macaque and human axons, however, did not reproduce the soma-based axonal properties, but showed a broader distribution of spine innervation from 0-80% spine preference (here and in the following, spine preference implies fraction of an axon's synapses established as single spine innervations, not considering doubly innervated spines).

What could yield this difference in axonal properties between soma-based and dense reconstructions in macaque and human? In particular we needed to understand the origin of axons with >40% spine targeting in macaque and human (Fig. 3E) that we had rarely observed in the soma-based reconstructions (Fig. 3B). Soma-based reconstructions in datasets smaller than the complete axonal arbor bias axonal reconstructions toward local (not distally located) neurons, and to the proximal parts of these neurons' axons. When analyzing the distance-dependence of axonal targeting properties for pyramidal axons from human (Fig. 3, G to I), we indeed found evidence for a substantial change from proximal axonal preference of shaft innervation to distal preference for spine innervation along the axon's path [(*64–66*) see (*67*) for a first report of such a path-length dependent synaptic sorting phenomenon along axons in the mammalian cerebral cortex and (*68*, *69*) for earlier reports in the bird brain]. We had to take this effect (Fig. 3, B, E, and I) into account when comparing the axonal properties in these species (Fig. 4).

Excitatory vs. inhibitory synaptic input balance

We first identified synapses onto a dendritic shaft of distal pyramidal cell dendrites and reconstructed the presynaptic axon from these synapses ("shaft-seeded" axons). Then we determined these axons' synaptic target properties based on their other output synapses (Fig. 4A). While in mouse, as expected, axons were clearly identifiable as excitatory vs. inhibitory based on their dichotomy in spine targeting preference (Fig. 4A), the distributions of axonal properties were much less distinct in human, recapitulating the properties of densely reconstructed axons in macaque and human (Fig. 4A; compared with Fig. 3, B and E). Because this data did not allow the simple threshold-based classification of axons into inhibitory vs. excitatory that can be used in mouse, we needed a more rigorous approach for axon type determination (Fig. 4, C to E).

We used the notion that the various types of axons and dendrites and their synaptic output and input properties in dense cortical neuropil are ultimately constrained by the synaptic composition of this neuropil volume (Fig. 4B). The volumetric density of synapses onto dendritic spines in the neuropil, for example, has to be composed by the intermixing of the spine preference of the various axon types present in the neuropil, and similarly for other types of synapses. Because dense 3-D EM data allowed us to concomitantly measure the properties of extended stretches of axons and dendrites together with the dense volumetric synaptic composition of the neuropil, we could determine the occurrence and target properties of excitatory and inhibitory axons without having to make prior assumptions about their relative prevalence (Materials and methods).

We built a model in which the synaptic properties of excitatory and inhibitory axons, and their relative prevalence were determined (Fig. 4, C and D): Inhibitory axons were modeled by a multinomial distribution based on point estimates for their synaptic target preferences, while for excitatory axons, a distribution of target preference was modeled by a Dirichlet-multinomial to account for the effects of broadened synaptic preference reported in Fig. 3, (Materials and methods). The model was fully constrained by the following input data, which we obtained from carefully curated expert reconstructions in all datasets (n=11,308 synapses annotated) (Fig. 4B): (1) volumetric fraction of spine synapses; (2) fraction of input synapses onto spines along spiny (ExN) dendrites; (3) fraction of output synapses onto spines along axons seeded from ExN dendritic spines; (4) fraction of output synapses onto spines along axons seeded from ExN dendritic shafts; (5) fraction of output synapses onto spines along axons seeded from IN (smooth) dendritic shafts. Note that these input data did not require a pre-hoc classification of the synapses or axons as inhibitory vs. excitatory, and did not contain the axons reconstructed from identified cell bodies (Fig. 3, A to C). With this input data, we obtained fits of the synaptic target properties of excitatory and inhibitory axons in each dataset (Fig. 4, C and D shown for mouse S1 and

Human STG datasets): point estimates for the fraction of synapses made onto ExN spines, ExN shafts and IN shafts for inhibitory axons (Fig. 4, C and D) and distributions of these target fractions for excitatory axons. Together with the modeled relative prevalence of inhibitory vs. excitatory synapses, for any axonal stretch with any combination of x synapses onto shaft and y synapses onto spine, we obtain a probability of this axon to be excitatory vs. inhibitory (Fig. 4, C and D, right). For validation of the model, we used the soma-based axon reconstructions (Fig. 3, A to C) for which we had certainty about their excitatory vs. inhibitory property, and sampled local stretches from these ground truth axons, and asked the model to predict their excitatory vs. inhibitory character (E→I and I→E misclassification rates: 0% and 0% for mouse, 6.9% and 8.4% for primates); (fig. S2 and supplementary materials, materials and methods).

We then applied the model to determine the expected inhibitory vs. excitatory synaptic properties of ExN dendrites in all datasets (bootstrapped to account for sample size in input data, and controlled for initial conditions; Methods) (Fig. 4E). We found that the inhibitory input balance increased only moderately from 9.3%±0.8% (mean±s.d.) in mouse to 13.8%±1.4% (P=0.001, bootstrap sampling) in macaque and human, revoking a setting in which the inhibitory to excitatory input balance were to change in proportion to the 2.5-fold increase in IN fraction from mouse to macaque and human (Fig. 4E; compare with Fig. 3C) (P=0.003; when also considering all other types of input synapses, P<0.001; bootstrap sampling, see Methods). Rather, the increased fraction of shaft input synapses coincided with a change in axonal targeting properties: excitatory axons made 0.7%±0.3% of their synapses onto ExN shafts in mouse, but 12.0%±1.1% in macaque and human (P<0.001, bootstrap), and their IN shaft targeting changed from 4.4%±0.7% to 17.3%±1.7% (P<0.001, bootstrap, consistent with the automated axon reconstructions).

This lack of enhanced inhibition onto ExN dendrites was also found for the proximal input domains of pyramidal cells (axon initial segment, soma and proximal dendrites), (fig. S1), excluding the possibility that inhibitory synapses had been redistributed toward the perisomatic domains.

These data yielded the important question where the expanded inhibitory population in human is establishing its synapses?

Properties of the expanded inhibitory neuronal network in human

To determine the inhibitory network properties in mouse vs. human we first applied a simple IN classification based on the configuration of IN dendrites as multipolar (MP) vs. non-multipolar (which included bipolar, bitufted, vertically oriented dendritic trees, (Fig. 5, A to D), labeled as "bipolar" (BP) for simplicity). The IN pool changed from dominated by multipolar INs in mouse (about 70-82% MP vs. 18-30% BP, n=52 vs. 17) (Fig. 5D)to a majority of bipolar INs in macaque/Human (53% BP; n=122 MP vs. n=135 BP, P<0.01, see methods for test) (Fig. 5D). When mapping the synaptic target properties of these classes of INs in mouse vs. human (Fig. 5, E and F), we found a fraction of bipolar (BP) INs with almost exclusive innervation of other INs in human that was not found in mouse (IN targeting by BP IN axons increased from 56% (Fig. 5, F and G)(70 IN targets out of 126 synapses, N=4 axons) to 72% (Fig. 5G)(225 IN targets out of 314 synapses, N=9 axons), P=0.018) (Materials and methods) (*63*). The changed IN pool composition together with the changed distribution of IN targeting properties would predict a substantial increase of IN-preferring inhibitory axons in the dense neuropil of human vs. mouse (Fig. 5F). In fact, when analyzing the target preferences of inhibitory axons for smooth (IN) dendrites in mouse vs. macaque and human from the dense automated reconstructions (Fig. 5H), we find a substantial shift toward interneuron-to-interneuron connectivity that can account for the inhibitory synapses contributed by the expanded IN pool in macaque and human (average smooth dendrite targeting probability of inhibitory axons: 8.0%±15.0% in mouse vs. 21.4%±29.0% in human; n=6565 vs. n=2048 axons; $P=2.2\times10^{-104}$, one-sided Kolmogorov-Smirnov test). Together with the increased interneuron fraction (Fig. 2B), this would estimate the IN-to-IN network to expand 6.7-fold from mouse to human. Based on the model (Fig. 4) we estimated the expansion to be 8.6-fold (from 1.0 ± 0.2% IN-IN connectivity in mouse to 8.6 ± 1.4% in macaque and human) (fig. S2F and supplementary materials, materials and methods).

To better understand the contributions of types of INs to this enhanced network, we then analyzed the synaptic input balance onto IN dendrites in MP and BP-INs in mouse, macaque and human (Fig. 5, I to K). To our surprise, already in mouse, MP-INs and BP-INs have different inhibitory input balance (Fig. 5, I and K): While MP-INs receive 7.6 ± 2.5% inhibitory input (bootstrapped mean±s.d.; n=105 axons from n=5 mouse datasets, n=977 synapses total), BP-INs receive 26.2 ± 5.0% (n=88 axons, n=694 synapses, P=0.001). In macaque and human, MP-INs receive inhibitory input that is commensurate to the fraction of INs in the cortex (24.2 ± 6.4%, n=69 axons from n=4 datasets, n=514 synapses; P=0.6 for scaling by IN fraction increase), while BP receive further enhanced inhibition (44.3 ± 7.8%, n=71 axons, n=506 synapses, P=0.026). These data indicate differential inhibitory targeting across species, and may imply separate IN-to-IN circuits to be substantially enhanced in macaque and human.

Excitatory synaptic network

Finally, we wanted to determine the magnitude of the synaptic input to pyramidal cells in human cortex. With the expanded size of pyramidal cell dendritic trees, it has been assumed that human pyramidal cells receive a larger number of input synapses than mouse pyramidal cells (from about 10,000 to about 30,000, (*15*, *29*, *43*, *44*, *46*). Because we found a strongly reduced spine-targeting synapse density in human cortex (Fig. 2E), we wondered what the quantitative input structure of human pyramidal cells would in fact be (Fig. 6, A and B, and figs. S1 and S4).

We used our large-scale 3D EM datasets obtained in one human individual that spanned the entire depth of cortical gray matter to reconstruct a substantial portion of L2/3 pyramidal cells. Based on these reconstructions, we extrapolated to the full extent of the dendritic tree. The large dataset extent in-plane allowed us to map some pyramidal cell dendrites in their full extent from soma to dendritic tip, and use the properties of these completely mapped dendrites for estimating the total path length of pyramidal cell dendrites in human (see Methods). The resulting estimates of total dendritic path length (about 9-20 mm path length, Fig. 6B and fig. S4) were consistent with light-microscopic reconstructions (*43*, *45*). Because we measured synaptic input density in parallel, we could exclude a compensation of lower dendritic path length by higher spine-targeting synapse density for individual pyramidal cells. Together, total synaptic input to pyramidal cells was 12,000-17,000 in human L2/3, far below an increase corresponding to the about 3-fold thicker cerebral cortex yielding about 3-fold larger pyramidal cell dendritic trees compared to mouse (Fig. 6B).

Discussion

The comparative analysis of mouse, macaque and human cortical neuronal networks revealed that the most substantial changes in neuronal architecture, the increase of pyramidal cell size and the numeric expansion of the interneuron pool, have not resulted in the most immediate possible circuit changes: neither an increase of total synaptic input on pyramidal cells, nor an overall shift of their synaptic input balance toward inhibition. Rather, we found an about 6-8-fold expanded interneuron-to-interneuron network in macaque and human cortex (Fig. 6C and fig. S2F). These circuit alterations point toward interneuron-to-interneuron connectivity as a key evolutionary change from mouse to primates including human.

Dependence of spine densities on age

Our finding of an almost constant total synaptic input to human pyramidal cells when compared to mouse may be affected by a reported age-dependent decline of dendritic spines in cortex (*70–72*) which could amount to a reduction in spine density of 45-48% during puberty (*72*). In fact, the human samples were from individuals in the upper quarter of expected life length. However, we found low spine densities in macaque, as well, at about 50% life expectancy. Similarly, rodents of 50-80% life expectancy show spine densities comparable to those reported here for younger mice (*55*, *67*). It is therefore unlikely that age-related effects have dominated the finding of reduced spine densities in human compared to mouse. Also, while temperature-dependent changes in spine densities have been reported (*73*), these are unlikely the cause of our measured spine densities (Fig. 2E and supplementary materials) (*29*, *44*, *46*, *55*, *66*, *74–77*)).

Synaptic strength vs. synaptic number

Our data indicates the maintenance of the relative number of inhibitory vs. excitatory input synapses on the dendrites of pyramidal cells in human vs. mouse. The effective balance between inhibition and excitation could be altered by different strength of synapses. Evidence for larger unitary EPSPs and for larger synapses and presynaptic vesicle pools has been found in experiments on human cortical slices (*16*, *30*, *78*, *79*). At the same time, the impact of single inhibitory synapses is enhanced (*19*, *20*). Whether synaptic number is a proper indicator of overall synaptic impact is a matter of investigation, with evidence in ferret (*80*) pointing toward a dominant effect of synapse number, as we quantified here.

Increased complexity of inhibitory networks

The interneuron-to-interneuron network expansion found in macaque and human could have a multitude of dynamic effects. While the most immediate consequence could be a more evolved disinhibitory network capability, for example for the gating of otherwise inhibited excitatory activity (*81*, *82*), theoretical studies have also indicated possible effects on the maintenance of working memory via enhanced interneuron-to-interneuron connectivity and the ensuing network dynamics (*83*). Our data indicate that a detailed investigation of such phenomena is required for an understanding of human cortex. In particular, alterations in interneuron-to-interneuron connectivity should become a focus of study in the context of possible pathological alterations of human cortex.

Methods

Animal experiments and human tissue samples

All animal-related experimental procedures were performed according to the law of animal experimentation issued by the German Federal Government under the supervision of local ethics committees and according to the guidelines of the Max Planck Society. Experimental procedures were approved by Regierungspräsidium Darmstadt,

AZ: F 126/1002 (mouse) and Regierungspräsidium Marburg AZ: V54 -19c 20 15 hours 01 MR 13/1 Nr. 78/2012 (macaque).

The human brain tissue samples were collected during neurosurgical procedures that were indicated for medical reasons and independently from this research project at the Department of Neurosurgery at the Klinikum rechts der Isar of the Technical University of Munich. They were obtained from access tissue (i.e., presumably healthy brain parenchyma that had to be removed as part of the procedure and would have been discarded otherwise) before removal of the respective target lesions, as approved by the Ethics Committee of the Technical University of Munich School of Medicine (Ethikvotum 184/16S and 273/21 S-EB). All patients had given their written informed consent.

The macaque brain tissue sample was collected at German Primate Center (DPZ) GmbH, Göttingen.

Tissue extraction and preparation

Mouse tissue was processed and imaged as described previously ((*49*, *55*, *84*). These consisted of four 3D-EM datasets from layers 2/3 of mouse somatosensory (S1), secondary visual (V2), posterior parietal (PPC) and anterior cingulate cortex (ACC) sized between 72 × 93 × 141 μm^3 and 88 × 56 × 213 μm^3 (Fig. 1) acquired at a voxel size of 11.24–12 × 11.24–12 × 28–30 nm^3 the present study densely reconstructed and reanalyzed these published datasets from mouse, together with a newly acquired dataset from mouse secondary auditory (A2) cortex. The published mouse dataset "PPC-2" (*55*) covering layers 1-5 was also used for expert reconstructions.

The human and macaque samples were processed as follows. All tissue specimen were fixed by either immersion (human) or transcardial perfusion (macaque) using an EM fixative composed of 2.5% paraformaldehyde (Sigma), 1.25% glutaraldehyde (Serva) and 2 mM calcium chloride (Sigma) in 80mM cacodylate buffer adjusted to pH 7.4 with an osmolarity ranging from 700 to 800 mOsmol/kg (*85*).

The human "H5" tissue was obtained from the right superior temporal gyrus of an 80 year old male patient during resection of a temporal mass lesion (final diagnosis: glioblastoma multiforme). After removal the sample was immersed in cold (13°C) EM fixative and transported to a nearby laboratory (transport time about 6 min). Partially submerged in cold fixative the sample was manually trimmed along the pia-WM axis and mounted on a vibratome stage. Then, submerged in cold EM fixative, the sample was cut into 500 µm thick slices with a vibratome (Leica VT 1200S). The slices were then transported in 8-12°C cooled fixative and stored over night at 4°C. The next day, samples spanning the entire cortical depth and about 1.5-1.7 mm in width were cut out and prepared for electron microscopy as described in (*55*) with the modification that the sample was embedded in Epon Hard for sectioning in the ATUM. For this, samples were infiltrated through a graded series (3:1 for 4h, 1:1 12h/overnight, 1:3 for 4h) of aceton and Epon resin (Epon hard mixture: 5.9 g Epoxy, 2.25 g DDSA, 3.7 g NMA, 205ul DMP; Sigma-Aldrich). Samples were then incubated in pure resin for 4h at room temperature, 12h/overnight at 4°, and another 4-5h at room temperature. Samples were directly embedded in pure resin on aluminum pins and kept in a pre-warmed oven (60°) for 2-3 days. Fresh resin was prepared for each incubation step.

The cured sample was trimmed into a hexagonal shape (size 3.1 mm × 1.8 mm) with a diamond milling head using an EM trimmer (Leica EM TRIM2, Leica Microsystems, Wetzlar, Germany). Next, the sample was cut into 35 nm to 40 nm thick slices at 0.3 mm s^{-1} cutting speed using a 4 mm ultra35° knife (DiATOME, Nidau, Switzerland). The ultrathin sections were collected on plasma-treated, carbon coated Kapton tape (custom-processed) with a customized ATUM-tome (RMC Boeckeler, Tucson, USA) (*51*, *52*). The tape was then mounted on silicon wafers using double-sided adhesive carbon tape (P77819-25, Science Services GmbH, Munich, Germany). In total, 7009 slices (corresponding to an extent of 270.25 µm) were cut.

The human "H6" sample was obtained from inferior frontal gyrus from a 69 year old female patient during surgical removal of frontal mass lesion (final diagnosis: glioblastoma multiforme). Following surgical removal, tissue was directly collected in fix solution kept at 4°C. The tissue was immediately sliced into 500 µm thin slices in cold fixative using vibratome. Slices were kept at 4°C overnight. Samples were then collected using 1mm circular medical biopsy punch (covering L2/3) and prepared for SBEM as described in (*55*).

The macaque sample was acquired from a 15.6 year old right handed male animal. Transcardial perfusion was performed under anesthesia (Ketamin, Xylazin) after an additional lethal dose of Barbituate (90-120 mg/kg i.v.). After flushing with ~2 l of 0.15 M cacodylate buffer (pH 7.4, duration 15 min) the perfusion solution was changed to ~2 l of EM fixative. The brain was removed and the anterior half of the brain was sectioned into 5 mm thick coronal sections. The sections were subsequently immersed in cold EM fixative, transported to the research laboratory and kept at 4°C over night. Within 48 hours the tissue was further dissected (with storage in 4°C EM fixative between processing steps). A ~5 mm wide tissue block centered on the anatomically defined arm/finger region of the left postcentral gyrus (Area 3a/b) medially adjacent to the rostral end of the intraparietal sulcus was dissected. The block was placed in 0.15 M cacodylate buffer and cut along the medio-lateral axis into 600 µm thick slices using a vibratome (Microm HM650V, Thermo Scientific). Using a medical biopsy punch (KAI medicals, USA), a 1.5 mm-wide sample spanning almost the entire thickness of the cortex was cut and subsequently prepared according to

the methods described in (*55*)using an automated tissue processor (Leica EM AMW).

3D EM imaging and image alignment

SBEM datasets of the human (H5, H6), macaque and mouse (A2) samples were acquired using a custom-built SBEM microtome ((*50*) courtesy of W. Denk) mounted inside the chamber of a scanning electron microscope (FEI Verios, Thermo Fisher Scientific, USA). The image acquisition and SBEM microtome were controlled using custom written software (*55*). Focus and stigmation were adjusted using custom written auto-correction routines. Imaging parameters were as follows: 4x6 (macaque, H5, H6) or 3x4 (mouse A2) mosaic tiles of images sized 4096 × 3536 voxels with an in-plane voxel size of $(11.24\ nm)^2$ and 30 nm nominal cutting thickness at 400 ns (macaque) or 700 ns (H5, H6, A2) dwell time with a nominal beam current of 800 pA (macaque) or 400 pA (H5, H6, A2).

Two Multi-SEM datasets of sample H5 were acquired as follows. In one experiment, 767 slices (476 at 35 nm, 291 at 40 nm) were imaged with a 61-beam MultiSEM (MultiSEM 505, Carl Zeiss Microscopy GmbH, Oberkochen, Germany) at a landing energy of 1.5 kV, a pixel size of 4 nm and a pixel dwell time of 50 ns with an FOV per slice of 1.7 mm × 2.1 mm. In a second experiment (H5_ext), 1342 additional slices (thickness 35-40 nm, corresponding to about 54 μm extent) were imaged with a smaller FOV per slice (1.1mm × 1.1mm) and aligned together with the previous experiment resulting in a total of 82 μm depth.

Image alignment for SBEM datasets was performed using global 3D relaxation of shift vectors calculated by SURF feature detection as in (*86*) followed by subimage alignment as in (*49*). The aligned image volume was then saved in the webKnossos (*87*) three-dimensional image format. Human H5 (STG), H6 (IFG), macaque (STG) and mouse (A2) SBEM datasets were aligned by scalable minds, Postdam, (supplementary materials, materials and methods) (*88*).

Image alignment for the two multiSEM datasets from sample H5 were performed similar to (*55*), following the alignment routines in (*89*) and https://github.com/bill-karsh/Alignment_Projects with modifications.

Cell type classification

For analyses in Fig. 2, A and B, cell bodies were manually annotated by an expert annotator in webKnossos (*87*). All cell bodies were identified and classified into pyramidal cell, interneuron and glia. Pyramidal cells were identified based on presence of an apical dendrite directed toward the pia, an axon initial segment directed toward the white matter, and spiny dendrites. Interneurons were identified based on their large somata, which contained large numbers of mitochondria, an axon often exiting from a dendrite, lack of a clear apical dendrite or, if presence of an apical-like dendrite, lack of basal dendrites and WM-directed AIS, and smooth dendrites. Non-neuronal cells were distinguished primarily by their smaller cell bodies and different nuclear shapes.

For distinction of multipolar vs. bipolar INs (Fig. 5, A to D), the dendrites of all identified interneurons were reconstructed and inspected in the coronal and tangential plane (*90–98*). Interneurons with short dendritic lengths were excluded from this classification.

Dendrite reconstructions

Pyramidal and interneuron dendrites (Fig. 2, D to G) were reconstructed by an expert annotator by following their trajectory throughout the dataset volume and placing nodes as described previously in (*55*, *84*). From these dendrites for which the identity of the originating cell body had been determined, a distal stretch of 3-49 μm length (mouse) and 7-44 μm length (macaque and human) was used for annotation of all input synapses.

Annotation of input synapses on dendrite, soma, axon initial segments

Analyses reported in Fig. 2, D to G, and fig. S1 were conducted as follows. For a given postsynaptic target class (dendrites, somata, or AIS), all input synapses were identified based on the presence of a presynaptic vesicle cloud and postsynaptic density [as described in (*55*, *67*, *84*); see following section]. These synapses were labeled as single spine when only one presynaptic bouton was found for a dendritic spine; double spine when two input synapses were found for which a clear distinction into primary (excitatory) and secondary (inhibitory) was not possible; primary spine and secondary spine when two input synapses were found for which this distinction was possible; neck for spine neck innervations, stubby spine synapses when a short dendritic protrusion of larger diameter than a spine neck and without clear diameter change at the end (i.e., no clear spine head) was synaptically innervated, and shaft synapses when the synapse was clearly placed on the main dendritic process without noticeable protrusion. Distances of synapses from the soma were measured using minimum spanning tree on the annotated nodes of the dendrites (see "skeleton" class in code repository).

Soma based axon reconstructions

Analyses reported in Figs. 3, A to C and G to I, and 5, E and F, were conducted as follows. The axons of identified pyramidal cell and interneurons were reconstructed by first identifying the exit at the axon initial segment (AIS). Then the trajectory of the axon was followed throughout the dataset and comments were added at the outgoing synapses. The post-target of each synapse was further classified into

excitatory or inhibitory class based on their spine-targeting synapse density (when target was dendritic) or cell body type (when target was a soma or an axon initial segment). Axons with fewer than 10 synapses were excluded to allow higher signal-to-noise ratio per axon.

Synapse-seeded axon reconstructions

Analyses reported in Fig. 4, A and B, were conducted as follows. For a given postsynaptic target with identified input synapses, a skeleton node was placed in the presynaptic axon's vesicle cloud and commented as "seed" synapse. The presynaptic axon was then reconstructed throughout the entire dataset volume, and all of the axons' other output synapses and their corresponding post-synaptic targets were identified as described in the following section. The "seed" synapse was excluded when quantifying axonal spine target properties in Fig. 4A.

Synapse identification for reconstructed axons

For analyses reported in Figs. 3, A to C and G to I; 4, A and B; and 5, E and F, the following synapse identification was applied. For each reconstructed axon, synapses were identified manually when following the trajectory of axon. First, vesicle clouds in the axon were identified as accumulations of vesicles. Subsequently, the most likely postsynaptic target was identified by the following criteria: direct apposition with vesicle cloud; presence of a darkening and slight broadening of the synaptic membrane; vesicles at close proximity to the plasma membrane at the site of potential synaptic contact. Synapses were marked as uncertain whenever the signs of darkened postsynaptic density could not be clearly identified. All analysis in this study were conducted only on synapses that had been classified as certain. For each axon, at every subsequent synapse location, a node was placed in the vesicle cloud and commented with the corresponding postsynaptic target's identity (i.e., if the postsynaptic target was soma, AIS, dendritic shaft, dendritic single spine, dendritic double-innervated spine, spine neck, stub, somatic spines or filopodium). All synapses were annotated by an expert annotator; for unclear cases, these were re-annotated for expert consensus between 2-3 experts.

Volumetric model of synapse and axon types, inference of synapse and axon types, automated reconstruction and error analysis

These methods are reported in the supplementary materials.

Estimates of total dendritic path length of human pyramidal cells

For the estimation of the complete synaptic input onto a L2/3 pyramidal cell (Fig. 6, A and B, and fig. S4), all dendrites of 10 L2/3 pyramidal cells were reconstructed until their end in dataset H5, which was either the actual ending of the dendrite in the neuropil, or the end of the dendrite at the dataset boundary (Fig. 6A). In addition, 9 pyramidal cells in the extended dataset H5_ext were analyzed with a larger fraction of in-dataset dendrite endings. Results from both datasets yielded similar ranges for total dendritic path length estimates, as detailed in the following.

For the following calculations, only dendrites with actual in-dataset endings were used (one exception were apical tuft dendrites in which some dendrites without in-dataset endings had more branch points and were therefore included in the estimate). This approach could correspond to an underestimation of dendrite length; therefore, in addition to the length measurements described here, we also used length reports from light-microscopically imaged human L3 pyramidal neurons, which provided similar path length measurements (ranges in Fig. 6B) (*45*).

For each pyramidal cell, the following dendritic compartments were distinguished: (i) apical dendrite trunk (measured from the exit at the cell body toward pia along the cortical axis, until the main bifurcation), (ii) apical tuft (measured from the main bifurcation point of the apical dendrite), (iii) oblique dendrites (measured from the exit at the apical dendritic trunk), and (iv) basal dendrites (all dendrites existing at the cell body except the apical dendrite) (*55*).

For the basal, oblique and apical tuft compartment N=226, 211, 167 dendrites were reconstructed of which N=25, 28 and 32 dendrites with in-dataset endings were found (N=21 cells).

For the estimation of the average number of branchpoints for the apical tuft compartment dendrites without in-dataset endings were included to avoid an underestimation of dendrite length as some of them had more branch points than the dendrites with in-dataset endings. For this, all apical tuft dendrites beyond a 300µm threshold were included (N=64 dendrites, with N=32 in-dataset endings, N=21 cells).

The estimations for the lengths of the above compartments were done as follows. The length for apical dendrite trunk compartment was estimated by averaging the lengths over all the samples from their soma exit until the main bifurcation. For each of the remaining compartments (i.e., apical tufts, oblique and basal dendrites), the path lengths ("PLs") between consecutive branch points ("BPs") were measured until a true end was reached. The order of a branch point ("order") was defined as the number of edges along the unique path between it and the cell body node (e.g., order is 0 at the cell body node, 1 at first branch point, 2 at second branch point and so on). Then for the entire compartment (i.e., apical tuft, oblique or a basal dendrite), the total length was calculated by summing the path lengths of each segment times 2 to the power order of the corresponding branch

point: $\sum_{order=0}^{BP} PL_{seg\_order} * 2^{order}$ where order = order of a branch point, BP = mean number of branch points for each compartment and PL_{seg_order} = path length of the succeeding segment at the corresponding branch point order. Then, the resulting total length of each compartment was multiplied with the average number of basal, oblique or apical tuft exits to estimate lengths for all basal, oblique and apical tufts respectively. The model of the branching as binary to the final branch point order would likely overestimate total dendritic path length, thus not affecting the conclusion about low total input synapse numbers in human.

To estimate the number of input synapses for each of the dendritic compartments, we proceeded as follows. For each compartment (i.e., apical trunk, apical tuft, oblique or basal dendrite), dendritic segments of path length 10-50 μm were sampled and all input synapses were annotated. For computing the spine-targeting synapse density per dendritic shaft path length, both single spine head and primary spine head synapses were included. For shaft synapse density, only the shaft synapses were included. For total synapse density, additionally secondary spine head, spine neck and dendrite "stub" synapses were included (total fraction of these additional synapses: less than 10%). The average spine, shaft and total synapse densities were then multiplied with the total path lengths of the corresponding compartments. The apical dendrite trunk was additionally distinguished into a proximal segment (up to 50 μm from cell body) and a distal segment (50 μm from soma until the main bifurcation). Similarly, the basal dendrites were additionally distinguished into a proximal segment which showed high shaft synapse density (up to 30 μm from cell body for mouse, 80 μm for human).

For the basal compartment we measured spine-targeting and shaft synapse densities of 0.66 ± 0.23 per μm and 0.23 ± 0.09 per μm (N=13), for the oblique compartment 0.67 ± 0.23 per μm and 0.19 ± 0.06 per μm (N=14), for the apical tuft compartment 0.73 ± 0.34 per μm (N=12) and 0.25 ± 0.07 per μm (N=12) respectively.

For the proximal segment of the apical trunk we measured spine-targeting and shaft synapse densities of 0.06 ± 0.14 per μm and 0.44 ± 0.16 per μm (N=9), for the distal segment until the main bifurcation 0.45 ± 0.39 per μm and 0.20 ± 0.08 per μm (N=7) respectively.

Statistical tests

All statistical tests were Kolmogorov-Smirnov for fractions and ratios, and Wilcoxon ranksum tests, otherwise. Data are shown as box or violin plots with median, 25th and 75th percentile and outliers (using MATLAB, Mathworks). All tests are documented in the code repository (see next section).

The test of significance for increase in interneuron fraction from mouse to macaque/human was done by pooling all identified excitatory neurons and interneurons counts per species group and generating 1000 bootstrap samples (*99*) with replacement. Interneuron fraction (IN_{frac}) was computed for each bootstrap sample. The *P*-value was calculated as the fraction of bootstrap samples in mouse for which IN_{frac} was greater than or equal to the lowest IN_{frac} in macaque/human bootstrap group (Fig. 2B, error bars 10th-90th percentiles). The same bootstrap approach was used as a test of significance for increase in non-multipolar IN fraction from mouse to macaque/human by pooling all multipolar and non-multipolar INs in volume per species group (Fig. 5D, error bars 10th-90th percentiles) and similarly for testing increase of interneuron-targeting fraction of non-multipolar IN axons from mouse to macaque/human by pooling all output synapses of non-multipolar IN axons per species group (Fig. 5, F and G).

Data availability

All electron microscopy datasets are publicly available for browsing at webknossos.org: Macaque L2/3 (S1), https://wklink.org/1186; Macaque L2/3 (STG), https://wklink.org/1319; Human (H5) L23 (STG), https://wklink.org/7861; Human (H5) L23 (STG) MultiSEM, https://wklink.org/5364; Human (H5) L1-6 (STG) MultiSEM, https://wklink.org/1742; Human (H6) L2/3 (IFG), https://wklink.org/7299; Mouse L2/3 (S1), https://wklink.org/9045; Mouse L2/3 (PPC), https://wklink.org/2581; Mouse L2 (ACC), https://wklink.org/7415; Mouse L2/3 (V2), https://wklink.org/3592; Mouse L2/3 (A2), https://wklink.org/7193; Mouse L1-5 (PPC-2), https://wklink.org/4814.

REFERENCES AND NOTES

1. S. Herculano-Houzel, The human brain in numbers: A linearly scaled-up primate brain. *Front. Hum. Neurosci.* **3**, 31 (2009). doi:10.3389/neuro.09.031.2009 Medline
2. C. S. von Bartheld, J. Bahney, S. Herculano-Houzel, The search for true numbers of neurons and glial cells in the human brain: A review of 150 years of cell counting. *J. Comp. Neurol.* **524**, 3865–3895 (2016). doi:10.1002/cne.24040 Medline
3. R. D. Hodge, T. E. Bakken, J. A. Miller, K. A. Smith, E. R. Barkan, L. T. Graybuck, J. L. Close, B. Long, N. Johansen, O. Penn, Z. Yao, J. Eggermont, T. Höllt, B. P. Levi, S. I. Shehata, B. Aevermann, A. Beller, D. Bertagnolli, K. Brouner, T. Casper, C. Cobbs, R. Dalley, N. Dee, S.-L. Ding, R. G. Ellenbogen, O. Fong, E. Garren, J. Goldy, R. P. Gwinn, D. Hirschstein, C. D. Keene, M. Keshk, A. L. Ko, K. Lathia, A. Mahfouz, Z. Maltzer, M. McGraw, T. N. Nguyen, J. Nyhus, J. G. Ojemann, A. Oldre, S. Parry, S. Reynolds, C. Rimorin, N. V. Shapovalova, S. Somasundaram, A. Szafer, E. R. Thomsen, M. Tieu, G. Quon, R. H. Scheuermann, R. Yuste, S. M. Sunkin, B. Lelieveldt, D. Feng, L. Ng, A. Bernard, M. Hawrylycz, J. W. Phillips, B. Tasic, H. Zeng, A. R. Jones, C. Koch, E. S. Lein, Conserved cell types with divergent features in human versus mouse cortex. *Nature* **573**, 61–68 (2019). doi:10.1038/s41586-019-1506-7 Medline
4. F. M. Krienen, M. Goldman, Q. Zhang, R. C H Del Rosario, M. Florio, R. Machold, A. Saunders, K. Levandowski, H. Zaniewski, B. Schuman, C. Wu, A. Lutservitz, C. D. Mullally, N. Reed, E. Bien, L. Bortolin, M. Fernandez-Otero, J. D. Lin, A. Wysoker, J. Nemesh, D. Kulp, M. Burns, V. Tkachev, R. Smith, C. A. Walsh, J. Dimidschstein, B. Rudy, L. S Kean, S. Berretta, G. Fishell, G. Feng, S. A. McCarroll, Innovations present in the primate interneuron repertoire. *Nature* **586**, 262–269 (2020). doi:10.1038/s41586-020-2781-z Medline
5. K. Letinic, R. Zoncu, P. Rakic, Origin of GABAergic neurons in the human neocortex. *Nature* **417**, 645–649 (2002). doi:10.1038/nature00779 Medline
6. S. R. y. Cajal, Estudios sobre la corteza cerebral humana. II. Estructura de la corteza motriz del hombre y mamíferos superiores. *Revista Trimestral Micrográfica* **4**, 117–200 (1899).
7. R. N. Kooijmans, W. Sierhuis, M. W. Self, P. R. Roelfsema, A quantitative comparison of inhibitory interneuron size and distribution between mouse and macaque V1, using calcium-binding proteins. *Cereb. Cortex Commun.* **1**, tgaa068 (2020). doi:10.1093/texcom/tgaa068 Medline
8. J. Berg, S. A. Sorensen, J. T. Ting, J. A. Miller, T. Chartrand, A. Buchin, T. E. Bakken, A. Budzillo, N. Dee, S.-L. Ding, N. W. Gouwens, R. D. Hodge, B. Kalmbach, C. Lee, B. R. Lee, L. Alfiler, K. Baker, E. Barkan, A. Beller, K. Berry, D. Bertagnolli, K. Bickley, J. Bomben, T. Braun, K. Brouner, T. Casper, P. Chong, K. Crichton, R. Dalley, R. de Frates, T. Desta, S. D. Lee, F. D'Orazi, N. Dotson, T. Egdorf, R. Enstrom, C. Farrell, D. Feng, O. Fong, S. Furdan, A. A. Galakhova, C. Gamlin, A. Gary, A. Glandon, J. Goldy, M. Gorham, N. A. Goriounova, S. Gratiy, L. Graybuck, H. Gu, K. Hadley, N. Hansen, T. S. Heistek, A. M. Henry, D. B. Heyer, D. Hill, C. Hill, M. Hupp, T. Jarsky, S. Kebede, L. Keene, L. Kim, M.-H. Kim, M. Kroll, C. Latimer, B. P. Levi, K. E. Link, M. Mallory, R. Mann, D. Marshall, M. Maxwell, M. McGraw, D. McMillen, E. Melief, E. J. Mertens, L. Mezei, N. Mihut, S. Mok, G. Molnar, A. Mukora, L. Ng, K. Ngo, P. R. Nicovich, J. Nyhus, G. Olah, A. Oldre, V. Omstead, A. Ozsvar, D. Park, H. Peng, T. Pham, C. A. Pom, L. Potekhina, R. Rajanbabu, S. Ransford, D. Reid, C. Rimorin, A. Ruiz, D. Sandman, J. Sulc, S. M. Sunkin, A. Szafer, V. Szemenyei, E. R. Thomsen, M. Tieu, A. Torkelson, J. Trinh, H. Tung, W. Wakeman, F. Waleboer, K. Ward, R. Wilbers, G. Williams, Z. Yao, J.-G. Yoon, C. Anastassiou, A. Arkhipov, P. Barzo, A. Bernard, C. Cobbs, P. C. de Witt Hamer, R. G. Ellenbogen, L. Esposito, M. Ferreira, R. P. Gwinn, M. J. Hawrylycz, P. R. Hof, S. Idema, A. R. Jones, C. D. Keene, A. L. Ko, G. J. Murphy, L. Ng, J. G. Ojemann, A. P. Patel, J. W. Phillips, D. L. Silbergeld, K. Smith, B. Tasic, R. Yuste, I. Segev, C. P. J. de Kock, H. D. Mansvelder, G. Tamas, H. Zeng, C. Koch, E. S. Lein, Human neocortical expansion involves glutamatergic neuron diversification. *Nature* **598**, 151–158 (2021). doi:10.1038/s41586-021-03813-8 Medline
9. T. E. Bakken, N. L. Jorstad, Q. Hu, B. B. Lake, W. Tian, B. E. Kalmbach, M. Crow, R. D. Hodge, F. M. Krienen, S. A. Sorensen, J. Eggermont, Z. Yao, B. D. Aevermann, A. I. Aldridge, A. Bartlett, D. Bertagnolli, T. Casper, R. G. Castanon, K. Crichton, T. L. Daigle, R. Dalley, N. Dee, N. Dembrow, D. Diep, S.-L. Ding, W. Dong, R. Fang, S. Fischer, M. Goldman, J. Goldy, L. T. Graybuck, B. R. Herb, X. Hou, J. Kancherla, M. Kroll, K. Lathia, B. van Lew, Y. E. Li, C. S. Liu, H. Liu, J. D. Lucero, A. Mahurkar, D. McMillen, J. A. Miller, M. Moussa, J. R. Nery, P. R. Nicovich, S.-Y. Niu, J. Orvis, J. K. Osteen, S. Owen, C. R. Palmer, T. Pham, N. Plongthongkum, O. Poirion, N. M. Reed, C. Rimorin, A. Rivkin, W. J. Romanow, A. E. Sedeño-Cortés, K. Siletti, S. Somasundaram, J. Sulc, M. Tieu, A. Torkelson, H. Tung, X. Wang, F. Xie, A. M. Yanny, R. Zhang, S. A. Ament, M. M. Behrens, H. C. Bravo, J. Chun, A. Dobin, J. Gillis, R. Hertzano, P. R. Hof, T. Höllt, G. D. Horwitz, C. D. Keene, P. V. Kharchenko, A. L. Ko, B. P. Lelieveldt, C. Luo, E. A. Mukamel, A. Pinto-Duarte, S. Preissl, A. Regev, B. Ren, R. H. Scheuermann, K. Smith, W. J. Spain, O. R. White, C. Koch, M. Hawrylycz, B. Tasic, E. Z. Macosko, S. A. McCarroll, J. T. Ting, H. Zeng, K. Zhang, G. Feng, J. R. Ecker, S. Linnarsson, E. S. Lein, Comparative cellular analysis of motor cortex in human, marmoset and mouse. *Nature* **598**, 111–119 (2021). doi:10.1038/s41586-021-03465-8 Medline
10. A. Shapson-Coe *et al.*, A connectomic study of a petascale fragment of human cerebral cortex. bioRxiv, 446289 [Preprint] (2021); doi:10.1101/2021.05.29.446289.
11. M. Field, I. P. Lukacs, E. Hunter, R. Stacey, P. Plaha, L. Livermore, O. Ansorge, P. Somogyi, Tonic $GABA_A$ receptor mediated currents of human cortical GABAergic interneurons vary amongst cell types. *J. Neurosci.* **41**, 9702–9719 (2021). doi:10.1523/JNEUROSCI.0175-21.2021 Medline
12. V. Szegedi, M. Paizs, J. Baka, P. Barzó, G. Molnár, G. Tamas, K. Lamsa, Robust perisomatic GABAergic self-innervation inhibits basket cells in the human and mouse supragranular neocortex. *eLife* **9**, e51691 (2020). doi:10.7554/eLife.51691 Medline
13. A. M. M. Sousa, Y. Zhu, M. A. Raghanti, R. R. Kitchen, M. Onorati, A. T. N. Tebbenkamp, B. Stutz, K. A. Meyer, M. Li, Y. I. Kawasawa, F. Liu, R. G. Perez, M. Mele, T. Carvalho, M. Skarica, F. O. Gulden, M. Pletikos, A. Shibata, A. R. Stephenson, M. K. Edler, J. J. Ely, J. D. Elsworth, T. L. Horvath, P. R. Hof, T. M. Hyde, J. E. Kleinman, D. R. Weinberger, M. Reimers, R. P. Lifton, S. M. Mane, J. P. Noonan, M. W. State, E. S. Lein, J. A. Knowles, T. Marques-Bonet, C. C. Sherwood, M. B. Gerstein, N. Sestan, Molecular and cellular reorganization of neural circuits in the human lineage. *Science* **358**, 1027–1032 (2017). doi:10.1126/science.aan3456 Medline
14. E. Boldog, T. E. Bakken, R. D. Hodge, M. Novotny, B. D. Aevermann, J. Baka, S. Bordé, J. L. Close, F. Diez-Fuertes, S.-L. Ding, N. Faragó, Á. K. Kocsis, B. Kovács, Z. Maltzer, J. M. McCorrison, J. A. Miller, G. Molnár, G. Oláh, A. Ozsvár, M. Rózsa, S. I. Shehata, K. A. Smith, S. M. Sunkin, D. N. Tran, P. Venepally, A. Wall, L. G. Puskás, P. Barzó, F. J. Steemers, N. J. Schork, R. H. Scheuermann, R. S. Lasken, E. S. Lein, G. Tamás, Transcriptomic and morphophysiological evidence for a specialized human cortical GABAergic cell type. *Nat. Neurosci.* **21**, 1185–1195 (2018). doi:10.1038/s41593-018-0205-2 Medline
15. J. DeFelipe, L. Alonso-Nanclares, J. I. Arellano, Microstructure of the neocortex: Comparative aspects. *J. Neurocytol.* **31**, 299–316 (2002). doi:10.1023/A:1024130211265 Medline
16. A. Rollenhagen, B. Walkenfort, R. Yakoubi, S. A. Klauke, S. F. Schmuhl-Giesen, J. Heinen-Weiler, S. Voortmann, B. Marshallsay, T. Palaz, U. Holz, M. Hasenberg, J. H. R. Lübke, Synaptic organization of the human temporal lobe neocortex as revealed by high-resolution transmission, focused ion beam scanning, and electron microscopic tomography. *Int. J. Mol. Sci.* **21**, 5558 (2020). doi:10.3390/ijms21155558 Medline
17. M. Domínguez-Álvaro, M. Montero-Crespo, L. Blazquez-Llorca, J. DeFelipe, L. Alonso-Nanclares, 3D electron microscopy study of synaptic organization of the normal human transentorhinal cortex and its possible alterations in Alzheimer's disease. *eNeuro* **6**, ENEURO.0140-19.2019 (2019). doi:10.1523/ENEURO.0140-19.2019 Medline
18. P. Marco, J. DeFelipe, Altered synaptic circuitry in the human temporal neocortex removed from epileptic patients. *Exp. Brain Res.* **114**, 1–10 (1997). doi:10.1007/PL00005608 Medline
19. B. Wang, L. Yin, X. Zou, M. Ye, Y. Liu, T. He, S. Deng, Y. Jiang, R. Zheng, Y. Wang, M. Yang, H. Lu, S. Wu, Y. Shu, A subtype of inhibitory interneuron with intrinsic persistent activity in human and monkey neocortex. *Cell Rep.* **10**, 1450–1458 (2015). doi:10.1016/j.celrep.2015.02.018 Medline
20. G. Molnár, S. Oláh, G. Komlósi, M. Füle, J. Szabadics, C. Varga, P. Barzó, G. Tamás, Complex events initiated by individual spikes in the human cerebral cortex. *PLOS Biol.* **6**, e222 (2008). doi:10.1371/journal.pbio.0060222 Medline
21. D. S. Melchitzky, S. R. Sesack, D. A. Lewis, Parvalbumin-immunoreactive axon terminals in macaque monkey and human prefrontal cortex: Laminar, regional,

and target specificity of type I and type II synapses. *J. Comp. Neurol.* **408**, 11–22 (1999). doi:10.1002/(SICI)1096-9861(19990524)408:1<11:AID-CNE2>3.0.CO;2-T Medline
22. M. Domínguez-Álvaro, M. Montero-Crespo, L. Blazquez-Llorca, J. DeFelipe, L. Alonso-Nanclares, 3D ultrastructural study of synapses in the human entorhinal cortex. *bioRxiv*, 2020.2005.2011.088435 (2020).
23. D. S. Melchitzky, D. A. Lewis, Dendritic-targeting GABA neurons in monkey prefrontal cortex: Comparison of somatostatin- and calretinin-immunoreactive axon terminals. *Synapse* **62**, 456–465 (2008). doi:10.1002/syn.20514 Medline
24. N. Cano-Astorga, J. DeFelipe, L. Alonso-Nanclares, Three-dimensional synaptic organization of layer III of the human temporal neocortex, three-dimensional synaptic organization of layer III of the human temporal neocortex. *Cereb. Cortex* **31**, 4742–4764 (2021). doi:10.1093/cercor/bhab120 Medline
25. B. G. Cragg, Ultrastructural features of human cerebral cortex. *J. Anat.* **121**, 331–362 (1976). Medline
26. I. B. Yáñez, A. Muñoz, J. Contreras, J. Gonzalez, E. Rodriguez-Veiga, J. DeFelipe, Double bouquet cell in the human cerebral cortex and a comparison with other mammals. *J. Comp. Neurol.* **486**, 344–360 (2005). doi:10.1002/cne.20533 Medline
27. E. A. Nimchinsky, E. Gilissen, J. M. Allman, D. P. Perl, J. M. Erwin, P. R. Hof, A neuronal morphologic type unique to humans and great apes. *Proc. Natl. Acad. Sci. U.S.A.* **96**, 5268–5273 (1999). doi:10.1073/pnas.96.9.5268 Medline
28. M. R. del Río, J. DeFelipe, Double bouquet cell axons in the human temporal neocortex: Relationship to bundles of myelinated axons and colocalization of calretinin and calbindin D-28k immunoreactivities. *J. Chem. Neuroanat.* **13**, 243–251 (1997). doi:10.1016/S0891-0618(97)00050-1 Medline
29. R. Benavides-Piccione, I. Ballesteros-Yáñez, J. DeFelipe, R. Yuste, Cortical area and species differences in dendritic spine morphology. *J. Neurocytol.* **31**, 337–346 (2002). doi:10.1023/A:1024134312173 Medline
30. V. Szegedi, M. Paizs, E. Csakvari, G. Molnar, P. Barzo, G. Tamas, K. Lamsa, Plasticity in Single Axon Glutamatergic Connection to GABAergic Interneurons Regulates Complex Events in the Human Neocortex. *PLOS Biol.* **14**, e2000237 (2016). doi:10.1371/journal.pbio.2000237 Medline
31. K. D. Micheva, C. Beaulieu, Postnatal development of GABA neurons in the rat somatosensory barrel cortex: A quantitative study. *Eur. J. Neurosci.* **7**, 419–430 (1995). doi:10.1111/j.1460-9568.1995.tb00338.x Medline
32. H. S. Meyer, D. Schwarz, V. C. Wimmer, A. C. Schmitt, J. N. D. Kerr, B. Sakmann, M. Helmstaedter, Inhibitory interneurons in a cortical column form hot zones of inhibition in layers 2 and 5A. *Proc. Natl. Acad. Sci. U.S.A.* **108**, 16807–16812 (2011). doi:10.1073/pnas.1113648108 Medline
33. D. Džaja, A. Hladnik, I. Bičanić, M. Baković, Z. Petanjek, Neocortical calretinin neurons in primates: Increase in proportion and microcircuitry structure. *Front. Neuroanat.* **8**, 103–103 (2014). Medline
34. B. Tasic, Z. Yao, L. T. Graybuck, K. A. Smith, T. N. Nguyen, D. Bertagnolli, J. Goldy, E. Garren, M. N. Economo, S. Viswanathan, O. Penn, T. Bakken, V. Menon, J. Miller, O. Fong, K. E. Hirokawa, K. Lathia, C. Rimorin, M. Tieu, R. Larsen, T. Casper, E. Barkan, M. Kroll, S. Parry, N. V. Shapovalova, D. Hirschstein, J. Pendergraft, H. A. Sullivan, T. K. Kim, A. Szafer, N. Dee, P. Groblewski, I. Wickersham, A. Cetin, J. A. Harris, B. P. Levi, S. M. Sunkin, L. Madisen, T. L. Daigle, L. Looger, A. Bernard, J. Phillips, E. Lein, M. Hawrylycz, K. Svoboda, A. R. Jones, C. Koch, H. Zeng, Shared and distinct transcriptomic cell types across neocortical areas. *Nature* **563**, 72–78 (2018). doi:10.1038/s41586-018-0654-5 Medline
35. J. Q. Ren, Y. Aika, C. W. Heizmann, T. Kosaka, Quantitative analysis of neurons and glial cells in the rat somatosensory cortex, with special reference to GABAergic neurons and parvalbumin-containing neurons. *Exp. Brain Res.* **92**, 1–14 (1992). doi:10.1007/BF00230378 Medline
36. C. Beaulieu, G. Campistron, C. Crevier, Quantitative aspects of the GABA circuitry in the primary visual cortex of the adult rat. *J. Comp. Neurol.* **339**, 559–572 (1994). doi:10.1002/cne.903390407 Medline
37. S. Lefort, C. Tomm, J. C. Floyd Sarria, C. C. H. Petersen, The excitatory neuronal network of the C2 barrel column in mouse primary somatosensory cortex. *Neuron* **61**, 301–316 (2009). doi:10.1016/j.neuron.2008.12.020 Medline
38. C. Beaulieu, Z. Kisvarday, P. Somogyi, M. Cynader, A. Cowey, Quantitative distribution of GABA-immunopositive and -immunonegative neurons and synapses in the monkey striate cortex (area 17). *Cereb. Cortex* **2**, 295–309 (1992). doi:10.1093/cercor/2.4.295 Medline
39. P. L. A. Gabbott, S. J. Bacon, Local circuit neurons in the medial prefrontal cortex (areas 24a,b,c, 25 and 32) in the monkey: I. Cell morphology and morphometrics. *J. Comp. Neurol.* **364**, 567–608 (1996). doi:10.1002/(SICI)1096-9861(19960122)364:4<567:AID-CNE1>3.0.CO;2-1 Medline
40. J.-P. Hornung, N. De Tribolet, Distribution of GABA-containing neurons in human frontal cortex: A quantitative immunocytochemical study. *Anat. Embryol.* **189**, 139–145 (1994). doi:10.1007/BF00185772 Medline
41. M. R. del Río, J. DeFelipe, Colocalization of calbindin D-28k, calretinin, and GABA immunoreactivities in neurons of the human temporal cortex. *J. Comp. Neurol.* **369**, 472–482 (1996). doi:10.1002/(SICI)1096-9861(19960603)369:3<472:AID-CNE11>3.0.CO;2-K Medline
42. E. G. Jones, G. W. Huntley, D. L. Benson, Alpha calcium/calmodulin-dependent protein kinase II selectively expressed in a subpopulation of excitatory neurons in monkey sensory-motor cortex: Comparison with GAD-67 expression. *J. Neurosci.* **14**, 611–629 (1994). doi:10.1523/JNEUROSCI.14-02-00611.1994 Medline
43. G. Eyal, M. B. Verhoog, G. Testa-Silva, Y. Deitcher, R. Benavides-Piccione, J. DeFelipe, C. P. J. de Kock, H. D. Mansvelder, I. Segev, Human cortical pyramidal neurons: From spines to spikes via models. *Front. Cell. Neurosci.* **12**, 181 (2018). doi:10.3389/fncel.2018.00181 Medline
44. R. Benavides-Piccione, I. Fernaud-Espinosa, V. Robles, R. Yuste, J. DeFelipe, Age-based comparison of human dendritic spine structure using complete three-dimensional reconstructions. *Cereb. Cortex* **23**, 1798–1810 (2013). doi:10.1093/cercor/bhs154 Medline
45. H. Mohan, M. B. Verhoog, K. K. Doreswamy, G. Eyal, R. Aardse, B. N. Lodder, N. A. Goriounova, B. Asamoah, A. B. C. B Brakspear, C. Groot, S. van der Sluis, G. Testa-Silva, J. Obermayer, Z. S. S. R. M. Boudewijns, R. T. Narayanan, J. C. Baayen, I. Segev, H. D. Mansvelder, C. P. J. de Kock, Dendritic and axonal architecture of individual pyramidal neurons across layers of adult human neocortex. *Cereb. Cortex* **25**, 4839–4853 (2015). doi:10.1093/cercor/bhv188 Medline
46. G. N. Elston, R. Benavides-Piccione, J. DeFelipe, The pyramidal cell in cognition: A comparative study in human and monkey. *J. Neurosci.* **21**, RC163–RC163 (2001). doi:10.1523/JNEUROSCI.21-17-j0002.2001 Medline
47. M. B. Ramocki, H. Y. Zoghbi, Failure of neuronal homeostasis results in common neuropsychiatric phenotypes. *Nature* **455**, 912–918 (2008). doi:10.1038/nature07457 Medline
48. J. L. R. Rubenstein, M. M. Merzenich, Model of autism: Increased ratio of excitation/inhibition in key neural systems. *Genes Brain Behav.* **2**, 255–267 (2003). doi:10.1034/j.1601-183X.2003.00037.x Medline
49. A. Motta, M. Berning, K. M. Boergens, B. Staffler, M. Beining, S. Loomba, P. Hennig, H. Wissler, M. Helmstaedter, Dense connectomic reconstruction in layer 4 of the somatosensory cortex. *Science* **366**, eaay3134 (2019). doi:10.1126/science.aay3134 Medline
50. W. Denk, H. Horstmann, Serial block-face scanning electron microscopy to reconstruct three-dimensional tissue nanostructure. *PLOS Biol.* **2**, e329 (2004). doi:10.1371/journal.pbio.0020329 Medline
51. K. J. Hayworth, J. L. Morgan, R. Schalek, D. R. Berger, D. G. C. Hildebrand, J. W. Lichtman, Imaging ATUM ultrathin section libraries with WaferMapper: A multi-scale approach to EM reconstruction of neural circuits. *Front. Neural Circuits* **8**, 68 (2014). doi:10.3389/fncir.2014.00068 Medline
52. K. J. Hayworth, N. Kasthuri, R. Schalek, J. W. Lichtman, Automating the collection of ultrathin serial sections for large volume TEM reconstructions. *Microsc. Microanal.* **12** (S02), 86–87 (2006). doi:10.1017/S1431927606066268
53. A. L. Eberle, S. Mikula, R. Schalek, J. Lichtman, M. L. K. Tate, D. Zeidler, High-resolution, high-throughput imaging with a multibeam scanning electron microscope. *J. Microsc.* **259**, 114–120 (2015). doi:10.1111/jmi.12224 Medline
54. K. Lee, J. Zung, P. Li, V. Jain, H. S. Seung, Superhuman accuracy on the SNEMI3D connectomics challenge. arXiv:1706.00120v1 [cs.CV] (2017).
55. A. Karimi, J. Odenthal, F. Drawitsch, K. M. Boergens, M. Helmstaedter, Cell-type specific innervation of cortical pyramidal cells at their apical dendrites. *eLife* **9**, e46876 (2020). doi:10.7554/eLife.46876 Medline

56. V. Braitenberg, A. Schüz, *Cortex: Statistics and Geometry of Neuronal Connectivity* (Springer Science & Business Media, 1998).
57. T. Kwon, A. Merchán-Pérez, E. M. Rial Verde, J.-R. Rodríguez, J. DeFelipe, R. Yuste, Ultrastructural, molecular and functional mapping of GABAergic synapses on dendritic spines and shafts of neocortical pyramidal neurons. *Cereb. Cortex* **29**, 2771–2781 (2019). doi:10.1093/cercor/bhy143 Medline
58. Y. Kubota, F. Karube, M. Nomura, Y. Kawaguchi, The diversity of cortical inhibitory synapses. *Front. Neural Circuits* **10**, 27–27 (2016). doi:10.3389/fncir.2016.00027 Medline
59. G. A. Wildenberg, M. R. Rosen, J. Lundell, D. Paukner, D. J. Freedman, N. Kasthuri, Primate neuronal connections are sparse in cortex as compared to mouse. *Cell Rep.* **36**, 109709 (2021). doi:10.1016/j.celrep.2021.109709 Medline
60. A. T. Kuan, J. S. Phelps, L. A. Thomas, T. M. Nguyen, J. Han, C.-L. Chen, A. W. Azevedo, J. C. Tuthill, J. Funke, P. Cloetens, A. Pacureanu, W. A. Lee, Dense neuronal reconstruction through x-ray holographic nano-tomography. *Nat. Neurosci.* **23**, 1637–1643 (2020). doi:10.1038/s41593-020-0704-9 Medline
61. Y. Kubota, S. Hatada, S. Kondo, F. Karube, Y. Kawaguchi, Neocortical inhibitory terminals innervate dendritic spines targeted by thalamocortical afferents. *J. Neurosci.* **27**, 1139–1150 (2007). doi:10.1523/JNEUROSCI.3846-06.2007 Medline
62. M. R. del Río, J. DeFelipe, A light and electron microscopic study of calbindin D-28k immunoreactive double bouquet cells in the human temporal cortex. *Brain Res.* **690**, 133–140 (1995). doi:10.1016/0006-8993(95)00641-3 Medline
63. I. P. Lukacs *et al.*, Differential effects of group III metabotropic glutamate receptors on spontaneous inhibitory synaptic currents in spine-innervating double bouquet and parvalbumin-expressing dendrite-targeting GABAergic interneurons in human neocortex. *bioRxiv*, 2022.2003.2005.483105 (2022).
64. C. Xu, H.-J. Liu, L. Qi, C.-L. Tao, Y.-J. Wang, Z. Shen, C.-L. Tian, P.-M. Lau, G.-Q. Bi, Structure and plasticity of silent synapses in developing hippocampal neurons visualized by super-resolution imaging. *Cell Discov.* **6**, 8 (2020). doi:10.1038/s41421-019-0139-1 Medline
65. G. M. Durand, Y. Kovalchuk, A. Konnerth, Long-term potentiation and functional synapse induction in developing hippocampus. *Nature* **381**, 71–75 (1996). doi:10.1038/381071a0 Medline
66. M. Lenz, P. Kruse, A. Eichler, J. Straehle, J. Beck, T. Deller, A. Vlachos, All-trans retinoic acid induces synaptic plasticity in human cortical neurons. *eLife* **10**, e63026 (2021). doi:10.7554/eLife.63026 Medline
67. H. Schmidt, A. Gour, J. Straehle, K. M. Boergens, M. Brecht, M. Helmstaedter, Axonal synapse sorting in medial entorhinal cortex. *Nature* **549**, 469–475 (2017). doi:10.1038/nature24005 Medline
68. J. Kornfeld, S. E. Benezra, R. T. Narayanan, F. Svara, R. Egger, M. Oberlaender, W. Denk, M. A. Long, EM connectomics reveals axonal target variation in a sequence-generating network. *eLife* **6**, e24364 (2017). doi:10.7554/eLife.24364 Medline
69. C. E. Carr, M. Konishi, A circuit for detection of interaural time differences in the brain stem of the barn owl. *J. Neurosci.* **10**, 3227–3246 (1990). doi:10.1523/JNEUROSCI.10-10-03227.1990 Medline
70. K. D. Micheva, C. Beaulieu, Quantitative aspects of synaptogenesis in the rat barrel field cortex with special reference to GABA circuitry. *J. Comp. Neurol.* **373**, 340–354 (1996). doi:10.1002/(SICI)1096-9861(19960923)373:3<340:AID-CNE3>3.0.CO;2-2 Medline
71. C. Calì, M. Wawrzyniak, C. Becker, B. Maco, M. Cantoni, A. Jorstad, B. Nigro, F. Grillo, V. De Paola, P. Fua, G. W. Knott, The effects of aging on neuropil structure in mouse somatosensory cortex-A 3D electron microscopy analysis of layer 1. *PLOS ONE* **13**, e0198131 (2018). doi:10.1371/journal.pone.0198131 Medline
72. J. P. Bourgeois, P. Rakic, Changes of synaptic density in the primary visual cortex of the macaque monkey from fetal to adult stage. *J. Neurosci.* **13**, 2801–2820 (1993). doi:10.1523/JNEUROSCI.13-07-02801.1993 Medline
73. S. A. Kirov, L. J. Petrak, J. C. Fiala, K. M. Harris, Dendritic spines disappear with chilling but proliferate excessively upon rewarming of mature hippocampus. *Neuroscience* **127**, 69–80 (2004). doi:10.1016/j.neuroscience.2004.04.053 Medline
74. L. A. Glantz, D. A. Lewis, Decreased dendritic spine density on prefrontal cortical pyramidal neurons in schizophrenia. *Arch. Gen. Psychiatry* **57**, 65–73 (2000). doi:10.1001/archpsyc.57.1.65 Medline
75. M. Medalla, J. P. Gilman, J.-Y. Wang, J. I. Luebke, Strength and diversity of inhibitory signaling differentiates primate anterior cingulate from lateral prefrontal cortex. *J. Neurosci.* **37**, 4717–4734 (2017). doi:10.1523/JNEUROSCI.3757-16.2017 Medline
76. A. Hsu, J. I. Luebke, M. Medalla, Comparative ultrastructural features of excitatory synapses in the visual and frontal cortices of the adult mouse and monkey. *J. Comp. Neurol.* **525**, 2175–2191 (2017). doi:10.1002/cne.24196 Medline
77. J. P. Gilman, M. Medalla, J. I. Luebke, Area-specific features of pyramidal neurons-a comparative study in mouse and rhesus monkey. *Cereb. Cortex* **27**, 2078–2094 (2017). Medline
78. A. Gidon, T. A. Zolnik, P. Fidzinski, F. Bolduan, A. Papoutsi, P. Poirazi, M. Holtkamp, I. Vida, M. E. Larkum, Dendritic action potentials and computation in human layer 2/3 cortical neurons. *Science* **367**, 83–87 (2020). doi:10.1126/science.aax6239 Medline
79. G. Eyal, M. B. Verhoog, G. Testa-Silva, Y. Deitcher, J. C. Lodder, R. Benavides-Piccione, J. Morales, J. DeFelipe, C. P. J. de Kock, H. D. Mansvelder, I. Segev, Unique membrane properties and enhanced signal processing in human neocortical neurons. *eLife* **5**, e16553 (2016). doi:10.7554/eLife.16553 Medline
80. B. Scholl, C. I. Thomas, M. A. Ryan, N. Kamasawa, D. Fitzpatrick, Cortical response selectivity derives from strength in numbers of synapses. *Nature* **590**, 111–114 (2021). doi:10.1038/s41586-020-03044-3 Medline
81. J. J. Letzkus, S. B. E. Wolff, E. M. M. Meyer, P. Tovote, J. Courtin, C. Herry, A. Lüthi, A disinhibitory microcircuit for associative fear learning in the auditory cortex. *Nature* **480**, 331–335 (2011). doi:10.1038/nature10674 Medline
82. J. J. Letzkus, S. B. E. Wolff, A. Lüthi, Disinhibition, a circuit mechanism for associative learning and memory. *Neuron* **88**, 264–276 (2015). doi:10.1016/j.neuron.2015.09.024 Medline
83. R. Kim, T. J. Sejnowski, Strong inhibitory signaling underlies stable temporal dynamics and working memory in spiking neural networks. *Nat. Neurosci.* **24**, 129–139 (2021). doi:10.1038/s41593-020-00753-w Medline
84. A. Gour, K. M. Boergens, N. Heike, Y. Hua, P. Laserstein, K. Song, M. Helmstaedter, Postnatal connectomic development of inhibition in mouse barrel cortex. *Science* **371**, eabb4534 (2021). doi:10.1126/science.abb4534 Medline
85. Y. Hua, P. Laserstein, M. Helmstaedter, Large-volume en-bloc staining for electron microscopy-based connectomics. *Nat. Commun.* **6**, 7923 (2015). doi:10.1038/ncomms8923 Medline
86. F. Drawitsch, A. Karimi, K. M. Boergens, M. Helmstaedter, FluoEM, virtual labeling of axons in three-dimensional electron microscopy data for long-range connectomics. *eLife* **7**, e38976 (2018). doi:10.7554/eLife.38976 Medline
87. K. M. Boergens, M. Berning, T. Bocklisch, D. Bräunlein, F. Drawitsch, J. Frohnhofen, T. Herold, P. Otto, N. Rzepka, T. Werkmeister, D. Werner, G. Wiese, H. Wissler, M. Helmstaedter, webKnossos: Efficient online 3D data annotation for connectomics. *Nat. Methods* **14**, 691–694 (2017). doi:10.1038/nmeth.4331 Medline
88. M. A. Fischler, R. C. Bolles, Random sample consensus: A paradigm for model fitting with applications to image analysis and automated cartography. *Commun. ACM* **24**, 381–395 (1981). doi:10.1145/358669.358692
89. L. K. Scheffer, B. Karsh, S. Vitaladevun, Automated alignment of imperfect EM images for neural reconstruction. arXiv:1304.6034v1 [q-bio.QM] (2013).
90. A. Peters, Cellular components of the cerebral cortex, in *Cerebral Cortex* (Univ. Chicago Press, 1984), vol. 1, pp. 107–200.
91. P. Somogyi, A. Cowey, Combined Golgi and electron microscopic study on the synapses formed by double bouquet cells in the visual cortex of the cat and monkey. *J. Comp. Neurol.* **195**, 547–566 (1981). doi:10.1002/cne.901950402 Medline
92. A. D. de Lima, J. H. Morrison, Ultrastructural analysis of somatostatin-immunoreactive neurons and synapses in the temporal and occipital cortex of the macaque monkey. *J. Comp. Neurol.* **283**, 212–227 (1989). doi:10.1002/cne.902830205 Medline
93. J. DeFelipe, S. H. Hendry, E. G. Jones, Synapses of double bouquet cells in monkey cerebral cortex visualized by calbindin immunoreactivity. *Brain Res.* **503**, 49–54 (1989). doi:10.1016/0006-8993(89)91702-2 Medline
94. J. DeFelipe, S. H. Hendry, T. Hashikawa, M. Molinari, E. G. Jones, A microcolumnar structure of monkey cerebral cortex revealed by immunocytochemical studies of double bouquet cell axons. *Neuroscience* **37**, 655–673 (1990). doi:10.1016/0306-4522(90)90097-N Medline

95. P. Somogyi, T. F. Freund, A. Cowey, The axo-axonic interneuron in the cerebral cortex of the rat, cat and monkey. *Neuroscience* **7**, 2577–2607 (1982). doi:10.1016/0306-4522(82)90086-0 Medline
96. B. Cauli, E. Audinat, B. Lambolez, M. C. Angulo, N. Ropert, K. Tsuzuki, S. Hestrin, J. Rossier, Molecular and physiological diversity of cortical nonpyramidal cells. *J. Neurosci.* **17**, 3894–3906 (1997). doi:10.1523/JNEUROSCI.17-10-03894.1997 Medline
97. Y. Kawaguchi, Y. Kubota, Physiological and morphological identification of somatostatin- or vasoactive intestinal polypeptide-containing cells among GABAergic cell subtypes in rat frontal cortex. *J. Neurosci.* **16**, 2701–2715 (1996). doi:10.1523/JNEUROSCI.16-08-02701.1996 Medline
98. C. K. Pfeffer, M. Xue, M. He, Z. J. Huang, M. Scanziani, Inhibition of inhibition in visual cortex: The logic of connections between molecularly distinct interneurons. *Nat. Neurosci.* **16**, 1068–1076 (2013). doi:10.1038/nn.3446 Medline
99. B. Efron, Bootstrap methods: Another look at the jackknife. *Ann. Stat.* **7**, 1–26 (1979). doi:10.1214/aos/1176344552
100. S. B. Hedges, S. Kumar, Genomics. Vertebrate genomes compared. *Science* **297**, 1283–1285 (2002). doi:10.1126/science.1076231 Medline
101. M. A. Hofman, Evolution of the human brain: When bigger is better. *Front. Neuroanat.* **8**, 15 (2014). doi:10.3389/fnana.2014.00015 Medline

ACKNOWLEDGMENTS

We thank K Mätz-Rensing at German Primate Center and F Bremmer and A Kaminiarz at University of Marburg for providing tissue of macaque brain, anonymous individuals H5 and H6 for consent to provide tissue from neurosurgery interventions, H Wissler for support with visualizations and for management of the neuron reconstruction team, I Wolf and J Kim for staining support, A Karimi, F Drawitsch and KM Boergens for providing custom written image acquisition and alignment routines, S Babl, L Bezzenberger, R Jakoby, R Kneisl and M Kronawitter for annotator training and task management, D Werner, V Pinkau, G Wiese, F Meinel, J Striebel, P Otto, T Herold and N Rzepka at scalable minds, Potsdam, Germany for collaboration on automated data analysis, and three anonymous reviewers for helpful advice. **Funding**: Funding was provided by the Max-Planck Society. SL was partly funded by Neuronex2 grant (DFG, German Research Foundation – HE 7321/1-1). **Author contributions:** MH conceived, initiated and supervised the study. JS, NH, AMK, VG and NJ carried out experiments. HSM and JG provided human tissue. MS provided ATUM-mSEM methodology. AM developed and applied analysis methodology. SL, JS, NH, AK, VG and MH provided reconstructions and analyzed data. SL and MH wrote the manuscript with contributions from all authors. **Competing interests:** The authors declare no competing financial interests. **Data and Materials availability:** All image data and reconstructions are publicly available via https://www.webknossos.org under the links at the end of the methods section. All software used for analysis is available at the following address and have been made publicly available under the MIT license. https://gitlab.mpcdf.mpg.de/connectomics/human_primate

SUPPLEMENTARY MATERIALS

science.org/doi/10.1126/science.abo0924
Materials and Methods
Supplementary Text
Figs. S1 to S4
MDAR Reproducibility Checklist

Submitted 13 January 2022; accepted 30 May 2022
Published online 23 June 2022
10.1126/science.abo0924

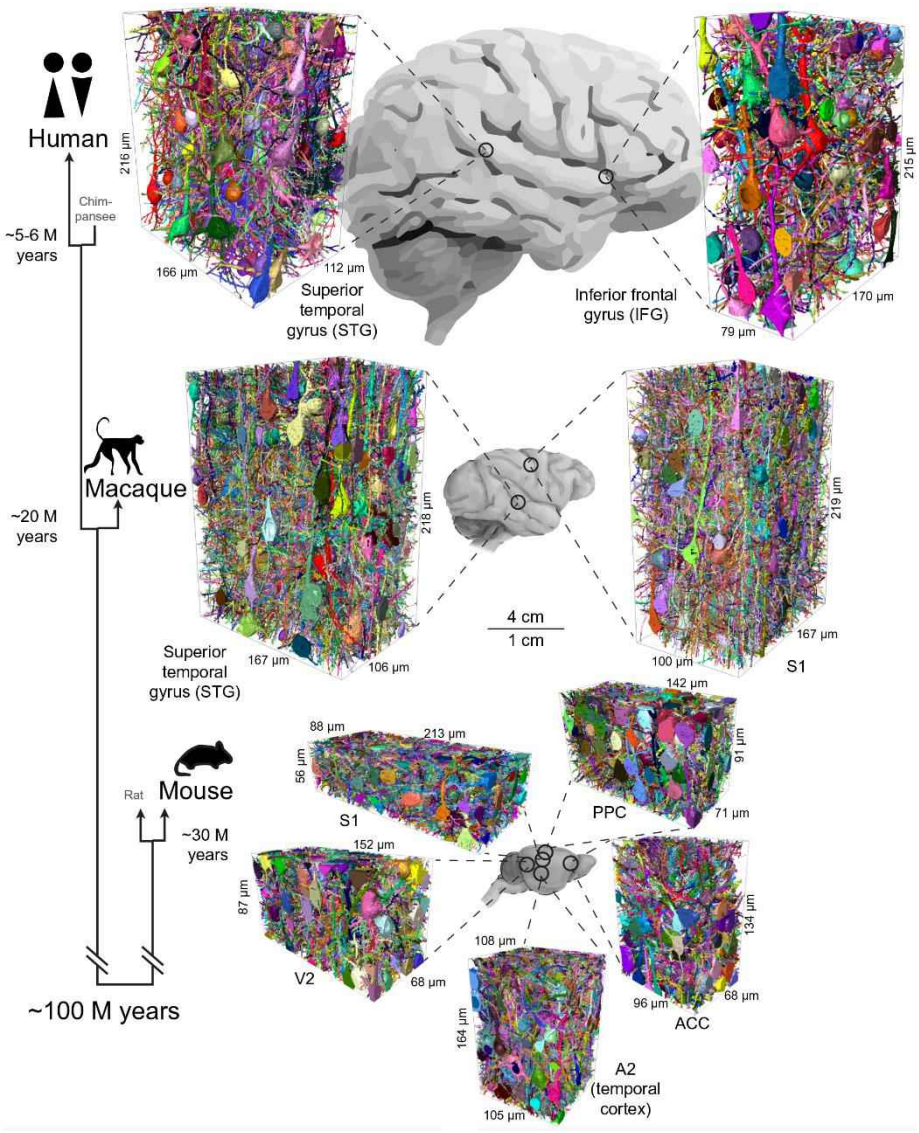

Fig. 1. Comparative connectomic analysis of mouse, macaque and human cortex. Dense connectomic reconstructions from layer 2/3 of 5 cortical areas of mouse (bottom, n=5 individuals) and from 4 cortical areas of macaque and human (n=3 individuals). Note matched cortical areas (A2, STG) across all 3 species, and paired samples from S1 (mouse, macaque). Total of 202,954 axons and 1,618,129 million synapses analyzed (see Methods). The raw 3D EM data of mouse datasets S1, V2, PPC and ACC were previously published (*55*), but not their dense reconstruction. Left, simplified phylogenetic tree [based on (*100*)] indicating time to last common ancestor between human (Homo sapiens) and rhesus macaque (Macaca mulatta), mouse (*Mus musculus*). Scale bars for brain sketches. S1, primary sensory cortex; A2, secondary auditory cortex; V2, secondary visual cortex; PPC, posterior parietal cortex; ACC, anterior cingulate cortex; STG, superior temporal gyrus; IFG, inferior frontal gyrus.

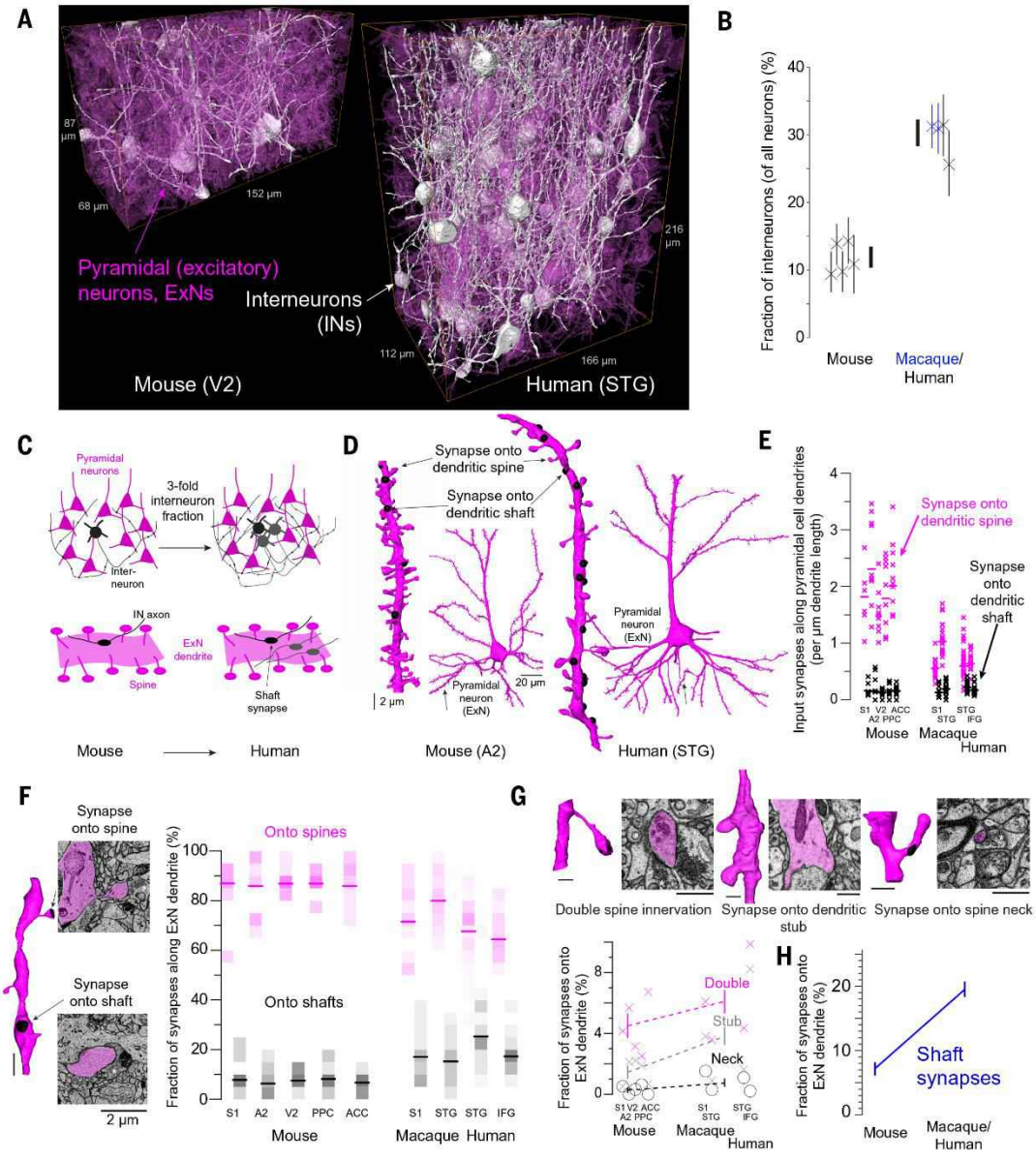

Fig. 2. **Multifold changes in cellular composition and synaptic input of mouse vs. macaque and human cortex.** (**A** and **B**) Reconstruction of excitatory neurons (ExN, magenta) and inhibitory interneurons (IN, white) shows 2.54-fold expansion of the interneuron pool from mouse to macaque and human, which (**C**) would predict a similar-fold increase in the inhibitory input onto ExNs, which would substantially alter the set point for the inhibitory vs. excitatory synaptic input balance in human compared to mouse. (illustrated for 3-fold increase). (**D** to **F**) Mapping of the synaptic input to excitatory neuron dendrites (D) showed an unaltered rate of shaft input synapses (E) but a 2.65-fold decrease of spine input synapses (E), resulting in a 2.72-fold increase in the fraction of input synapses made onto dendritic shafts (F). (**G**) Other dendritic inputs were rare but slightly increased from mouse to macaque and human: doubly innervated spines: 4.49 ± 0.01 vs. 4.68 ± 0.01 and 6.91 ± 0.01%; stub synapses: 1.44 ± 0.00 vs 2.17 ± 0.01 and 4.71 ± 0.01%; spine neck innervations: 0.26 ± 0.00 vs 0.84 ± 0.00 and 0.67 ± 0.00%, n=1111, 598, 1040 total synapses, respectively. Insets in F,G: EM images of example synapses from Human STG multiSEM-imaged (F); Macaque STG, Human IFC and Macaque S1, respectively (left to right in G). (**H**) Concomitant increase of shaft synapse input could support the altered i/e balance model in C, if axonal properties remain unchanged from mouse to macaque and human, analyzed in Figs. 3 and 4. Scale bars, 1 µm unless indicated otherwise. Data in A from automated reconstructions, in B, D-H from expert reconstructions.

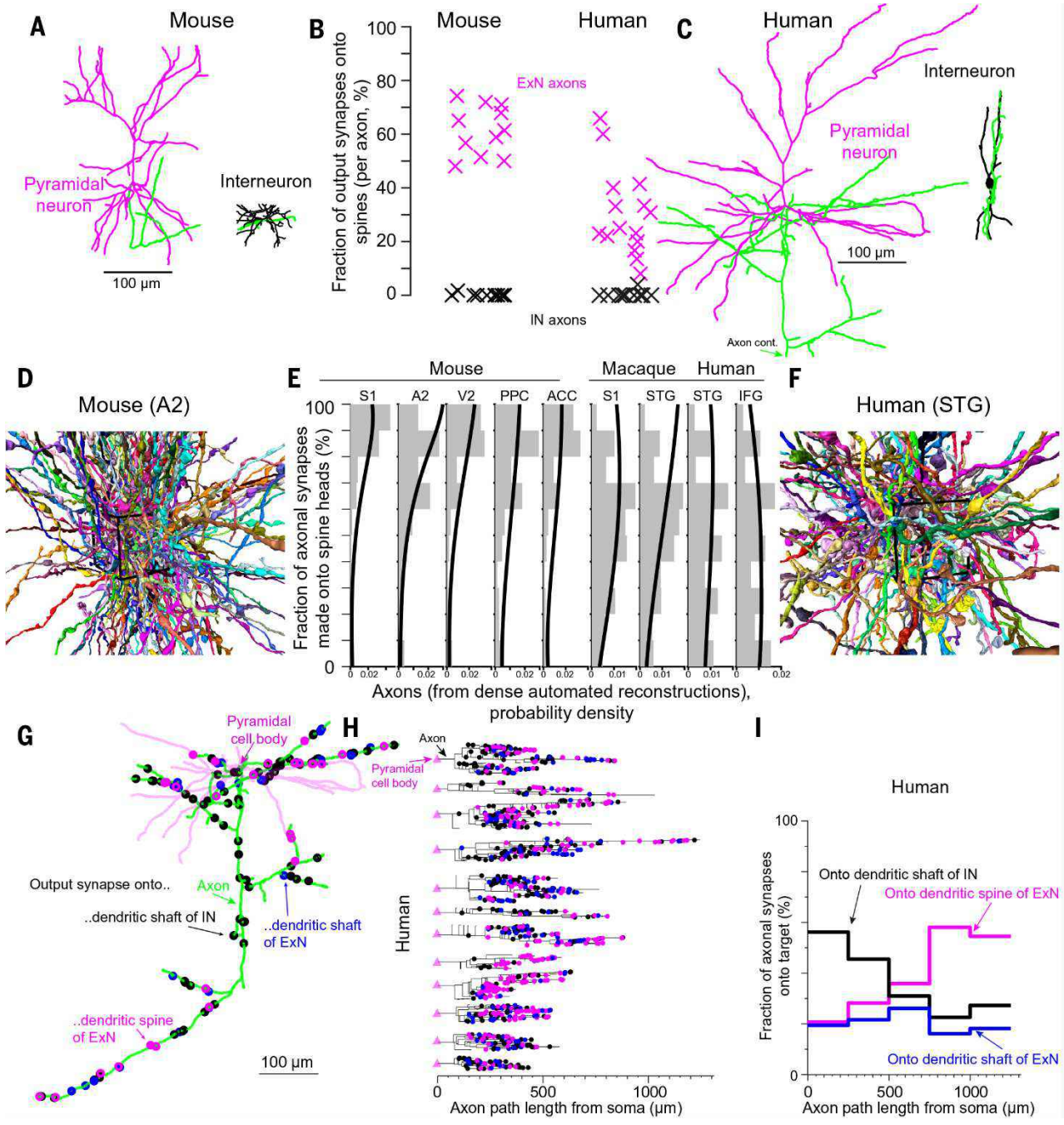

Fig. 3. Synaptic target properties of excitatory and inhibitory neurons in mouse and human. (**A** to **C**) Axonal target properties from identified pyramidal cells and interneurons (n=50 neurons, n=2101 output synapses, cross-validated expert reconstructions, see wklink.org/7881 and wklink.org/3103 (mouse), wklink.org/9448 and wklink.org/2204 (human) for all reconstructions). Absence of single spine innervation for interneurons in mouse and human (B), but shift in spine innervation of excitatory axons from mouse to human, yielding a less separated synaptic preference of excitatory vs. inhibitory axons. (**D** to **F**) Axonal target properties from dense axonal reconstructions in mouse, macaque and human. Examples of dense axon populations from mouse A2 (D) and Human STG (F), all axons traversing boxes of 10x10x10 μm^3 size shown (n=120 and n=89, respectively). Quantifications in (E) are based on all axons in the respective datasets (n=202,954 axons with 5 to 25 output synapses each; n=1,618,129 synapses). Gray, distribution of spine target fraction for all axons in the datasets, uncorrected. Black lines, average likelihood function of true spine target fraction under consideration of error rates (see methods). Broadening of axon target property distribution toward lower spine targeting in primate/human compared to mouse, that is however less pronounced than in soma-based axon reconstructions (B). (**G** to **I**) Path-length dependent axonal synapse sorting (PLASS) as a possible origin of broader axonal target property distributions in human. Example of pyramidal cell axon (G) from Human STG (path length: 3.74 mm, n=132 output synapses; same neuron as shown in C). Colors indicate synaptic target of axonal output synapses. [(H) and (I)] Distribution of axonal output synapses along pyramidal cell axons from human STG (n=15 axons, 1126 output synapses, expert reconstructions, n=12 reconstructions from mSEM dataset shown, for 3 axons from SBEM dataset see wklink.org/9448 and wklink.org/2204). Synapse symbols as in (G). Substantial increase in targeting of ExN spines over axonal path length (I). Data in A-C, G-I from expert reconstructions, D-F from dense reconstructions.

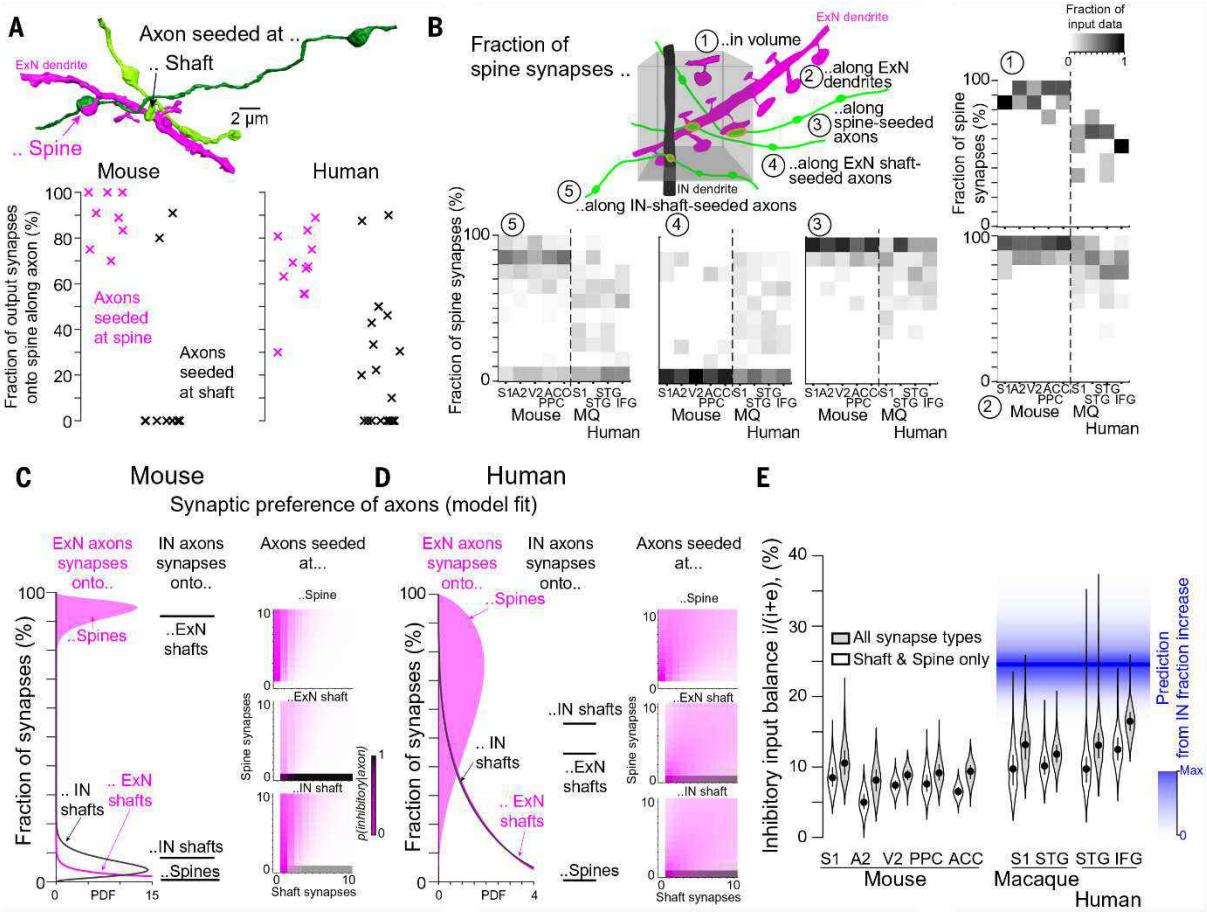

Fig. 4. Detailed analysis of inhibitory/excitatory input balance onto ExN dendrites. (A) Target properties of axons seeded at dendritic spines and shafts of ExN dendrites in mouse and human. Top, example reconstruction (Macaque STG), bottom, data from expert reconstructions in mouse S1 and Human STG (n=53 axons, n=626 output synapses) showing shift of axonal targeting analogous to densely reconstructed axons in mouse vs. human (compare Fig. 3E). (B to D) Model incorporating dense volumetric synapse densities together with dendritic and axonal targeting properties, but not using any assumption about excitatory vs. inhibitory synapses or axons: input data (B) from expert annotations (n=754 axons, n=11,308 synapses total) that fully constrain the model (C,D) (see Results and Methods; for model validation see Suppl. Figure S2). Shaded magenta curve: distribution of spine targeting by ExN axons; Magenta line: ExN shaft targeting by ExN axons; black line: IN shaft targeting by ExN axons; showing broadening of ExN axons' spine targeting fraction and shift of excitatory and inhibitory shaft targeting from mouse to human. MQ: macaque. (E) Resulting estimates of inhibitory input fraction (i/(i+e) balance) onto ExN dendrites in mouse, macaque and human. Violin plots represent expected inhibitory input synapse fraction along ExN dendrites (distribution across n=1000 bootstrap samples per dataset). Open shading: only shaft and single spine inputs considered; gray shading: including multiply innervated spines and other inputs, see Fig. 2G. Synaptic input balance does not approach the inhibitory bias predicted by the increased fraction of INs in macaque and human (blue shading indicates prediction from mouse to macaque and human, 24.9%±3.2% (mean±s.d.); p<0.001, by bootstrap sampling; see Methods). All data from expert reconstructions.

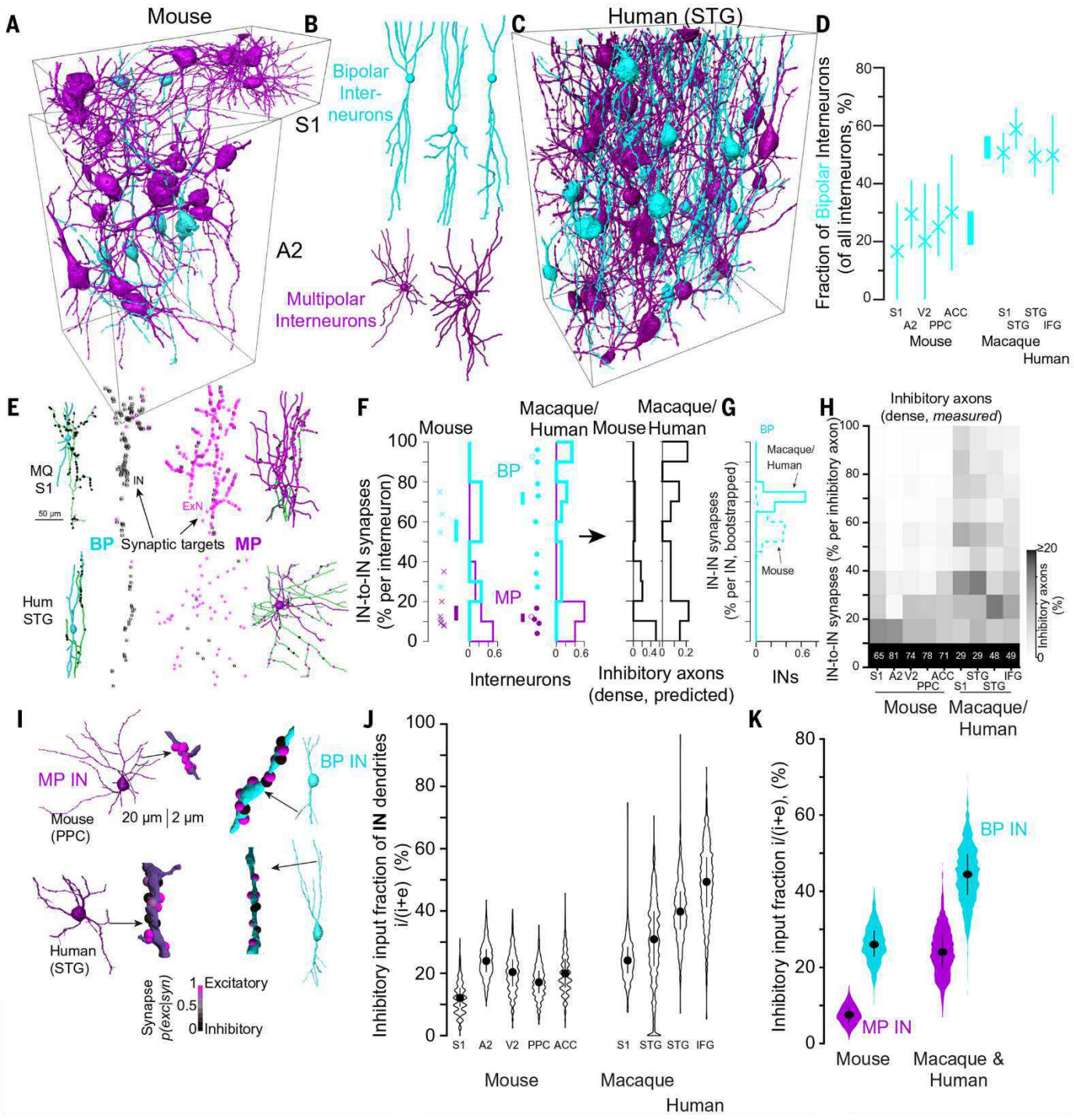

Fig. 5. Selective expansion of interneuron types and its effect on the inhibitory-to-inhibitory network. (**A** to **C**) Dense reconstruction of all interneurons in mouse (A) and human (C) with labeling of multipolar (MP, purple, B) vs. non-multipolar (BP, bipolar, bitufted, cyan, B) interneurons showing sparsity of BP interneurons in mouse (A) compared to human (C). (**D**) Proportion of BP interneurons 2.3-fold expanded from mouse to macaque and human. (**E**) Synaptic targets of BP vs. MP interneurons in macaque and human show selectivity for inhibitory (93% of synaptic targets, left) vs excitatory (87% of synaptic targets, right) postsynaptic partners. (**F**) Broader distribution of interneuron innervation selectivity in macaque and human vs. mouse from soma-based axon reconstructions. This predicts expansion of inhibitory-to-inhibitory connectivity in macaque/human vs. mouse (right panels). (**G**) Within the BP INs, IN targeting is further enhanced (from 56.63 ± 4.46% to 71.67 ± 2.48%, $p<0.05$, bootstrapped from 126 and 314 synapses respectively for mouse vs macaque and human). (**H**) Analysis of densely reconstructed inhibitory axons and their targeting of interneuron dendrites (n=94,391 synapses, n=11,384 axons) by inference of the most likely smooth dendrite targeting probability under consideration of the error rates of automated synapse detection. Expansion of IN-to-IN connectivity as predicted from soma-based reconstructions (F). (**I** to **K**) Detailed analysis of inhibitory input balance to MP vs. BP IN subtypes across species. (I) example reconstructions of input synapses onto IN dendrites. (J) Inhibitory input determined from the model in Fig. 4 for interneuron dendrites. 2.35-fold increase from mouse to human (18.9%±2.5% to 44.5%±7.3%, mean±s.d.) consistent with the prediction from IN expansion for IN dendrites ($p=0.662$). (J,K) Separate analysis of inhibitory input to MP vs. BP INs reveals difference in inhibitory input already in mouse (7.6% vs. 26.2%, $p=0.001$) that is further enhanced in macaque and human (24.2% vs. 44.3%, $p=0.026$). Data in H from dense reconstructions, otherwise expert reconstructions.

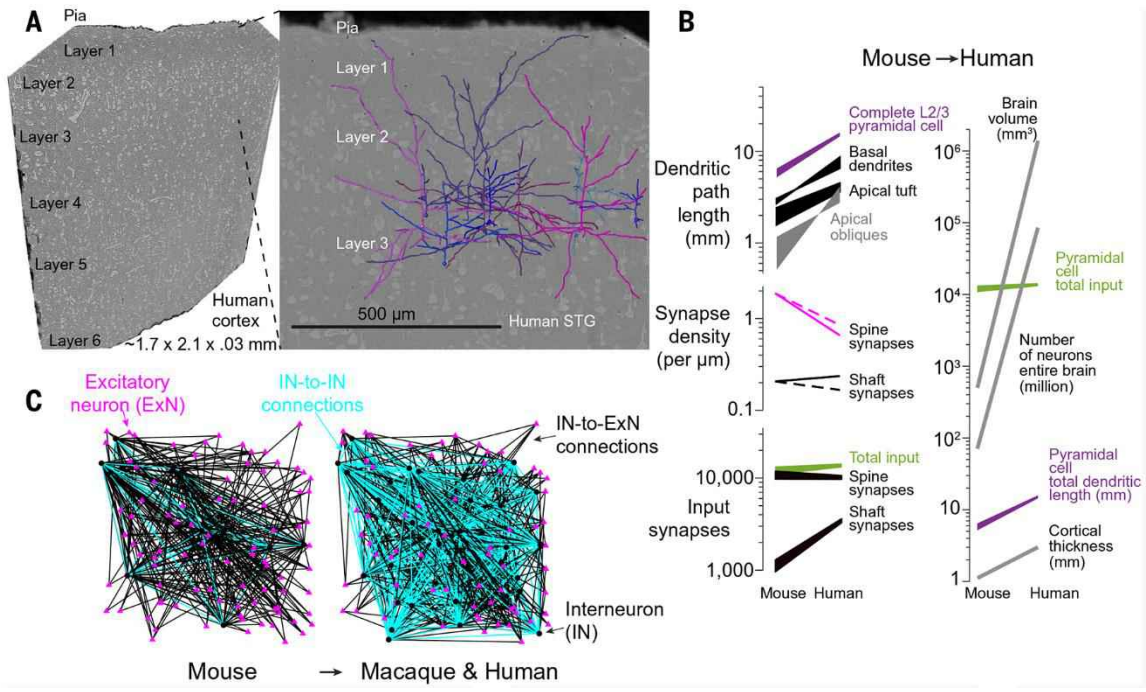

Fig. 6. Scaling of pyramidal cell synaptic input and network properties from mouse to human. (**A**) Large-scale 3D EM dataset spanning all cortical layers from human cortex (STG) for reconstruction of dendritic arbors of L2/3 pyramidal neurons. (**B**) With about 3-fold reduced spine density from mouse to human, the about 3-fold increase in pyramidal cell dendritic path length yields only moderately increased number of input synapses for human pyramidal cells compared to mouse. Dashed lines, macaque. (**C**) Expanded IN-to-IN network, illustrated based on model fit (Fig. 4, Suppl. Figure S2F, Suppl. Methods). Note 8.6-fold expansion of IN-to-IN connectivity from mouse to macaque and human. Data in A,B from expert reconstructions. In B right, lower limits of pyramidal cell total dendritic length and total input based on (*45*), upper limits based on data in current study. Brain volume based on (*101*), number of neurons in entire brain based on (*1*).

Connectomic comparison of mouse and human cortex

Sahil LoombaJakob StraehleVijayan GangadharanNatalie HeikeAbdelrahman KhalifaAlessandro MottaNiansheng JuMeike SieversJens GemptHanno S. MeyerMoritz Helmstaedter

Science, **Ahead of Print** • DOI: 10.1126/science.abo0924